

1.000
11-11-1994
C. J. Jobson
11-11-1994

A reprint from

OPTICAL ENGINEERING

March 1995

ISSN 0091-3286

ELECTRO-OPTICAL DESIGN FOR EFFICIENT VISUAL COMMUNICATION

Friedrich O. Huck
Carl L. Fales
Daniel J. Jobson

NASA Langley Research Center
Hampton, Virginia 23681
E-mail: f.o.huck@larc.nasa.gov

Zia-ur Rahman

Science and Technology Corporation
Hampton, Virginia 23666

Electro-optical design for efficient visual communication

Friedrich O. Huck, MEMBER SPIE

Carl L. Fales

Daniel J. Jobson

NASA Langley Research Center

Hampton, Virginia 23681

E-mail: f.o.huck@larc.nasa.gov

Zia-ur Rahman

Science and Technology Corporation

Hampton, Virginia 23666

Abstract. Visual communication, in the form of telephotography and television, for example, can be regarded as efficient only if the amount of information that it conveys about the scene to the observer approaches the maximum possible and the associated cost approaches the minimum possible. Elsewhere we have addressed the problem of assessing the end-to-end performance of visual communication systems in terms of their efficiency in this sense by integrating the critical limiting factors that constrain image gathering into classical communication theory. We use this approach to assess the electro-optical design of image-gathering devices as a function of the f number and apodization of the objective lens and the aperture size and sampling geometry of the photodetection mechanism. Results show that an image-gathering device that is designed to optimize information capacity performs similarly to the human eye. For both, the performance approaches the maximum possible, in terms of the efficiency with which the acquired information can be transmitted as decorrelated data, and the fidelity, sharpness, and clarity with which fine detail can be restored.

Subject terms: electro-optical design; information; entropy; dynamic-range compression; image coding; image restoration.

Optical Engineering 34(3), 795-813 (March 1995).

1 Introduction

The problem of visual communication is that of producing an image that conveys information to the human observer at one point about a scene that is located at another point. Until recently, in telephotography and television, for example, the input terminal of the visual communication channel consisted solely of the image-gathering device that transforms the spatially varying radiance field reflected or emitted by the scene into the signal that is transmitted, and the output terminal consisted solely of the image display device that transforms the received signal into an image. However, advances in technology are leading to rapid growth in the capabilities of analog and digital VLSI processors, even as their cost, size, weight, and power consumption decrease. Consequently, visual communication is now increasingly carried out by combining image gathering and display with digital image processing. Image gathering is combined with encoding to reduce data transmission, and image display is combined with restoration to enhance image quality. So far, however, the electro-optical design of image-gathering devices and the digital image processing for encoding and restoration have remained independent disciplines, following distinctly separate traditions.

The electro-optical design of image-gathering devices ordinarily revolves around two interdependent trade-offs. One trade-off, in terms of geometrical optics, is widely understood. It deals with instantaneous field of view (IFOV) versus

signal-to-noise ratio (SNR) as controlled largely by the aperture size and focal length of the objective lens together with the aperture size and responsivity of the photodetection mechanism.^{1,2} Additional factors that may enter into this trade-off are field of view, depth of field, and exposure time.³ The IFOV and associated sampling lattice that evolve from this trade-off establish the angular resolution, or spatial scale, of the visual communication, ranging from telescopic to microscopic.

The other trade-off, in terms of physical optics, which we address in this paper, is less widely understood. It deals with the relationship between the spatial-frequency response (SFR) of the optical (objective lens and photosensor) apertures and the sampling passband of the photodetection mechanism as a function of the SNR. The design that evolves from this trade-off establishes upper bounds on the information capacity of the visual communication channel at the spatial scale fixed by the sampling lattice.

Traditionally, the relationship between the SFR and sampling passband of the image-gathering device has been optimized to produce the best possible picture when the image display device reconstructs the received signal into an image without digital processing.⁴⁻⁶ For this reconstruction it is ordinarily preferred to let the SFR extend far beyond the sampling passband in order to avoid substantial blurring within the passband, at the cost of aliasing that the resultant insufficient sampling causes. However, the model of image gathering that has been used in the prevalent digital-image-processing literature⁷⁻¹² takes account only of blurring and noise. The insufficient sampling has been ignored both in the assessment of digital image coding (e.g., by rate distortion theory) and in the formulation of digital image restoration algorithms (e.g., the Wiener filter). This failure to take full

Paper 49044 received Apr. 29, 1994; revised manuscript received Oct. 17, 1994; accepted for publication Oct. 18, 1994. This paper is a revision of a paper presented at the SPIE conference on Visual Information Processing III, April 1994, Orlando, Fla. The paper presented there appears (unrefereed) in SPIE Proceedings Vol. 2239. © 1995 Society of Photo-Optical Instrumentation Engineers. 0091-3286/95/\$6.00.

account of the image-gathering process has seriously impeded the performance of visual communication systems in which image gathering and display are combined with digital image processing.

To overcome this impediment, Fales and Huck¹³ have developed a mathematical foundation for assessing the end-to-end performance of visual communication systems by rigorously integrating the critical limiting factors that constrain image gathering into the classical communication theories of Shannon¹⁴ and Wiener.¹⁵ These theories deal, respectively, with the efficient transmission of information through a noisy communication channel and the minimum-mean-squared-error restoration of the input signal to the channel from the received signal. The inclusion of the image-gathering constraints into these theories allows the designer to assess visual communication in terms of three intuitively attractive criteria: the information capacity of the image-gathering device, the theoretical minimum data rate at which the acquired information can be transmitted, and the maximum fidelity with which an image can be restored from the received data. It is an agreeable consequence of this approach¹⁶⁻¹⁸ that the image-gathering device that is designed to maximize the information capacity also tends to maximize the information efficiency with which decorrelated data can be transmitted and the sharpness and clarity as well as the fidelity with which images can be restored with the Wiener filter.

In addition to the spatial properties of the radiance field, the designer must often deal with its wide dynamic range. Radiance fields in natural terrestrial environments exhibit dynamic variations up to $10^{11} : 1$, ranging from the darkest visible extended surface to the brightest patches that one commonly encounters.¹⁹ The dynamic range of photosensors is substantially lower. For photosensor arrays, such as charge-coupled devices (CCDs), the dynamic range is $\sim 10^4 : 1$, ranging from the noise level to the highest signal level. The preamplifier that reads the signal out of the photosensor array to the analog-to-digital converter further limits the dynamic range to $\sim 3 \times 10^3 : 1$. The dynamic range of image display media is still lower. For film transparencies it may approach $10^3 : 1$, but for film prints it is only $\sim 10 : 1$, ranging from a reflectance of $\approx 0.8\%$ to 80% . Within this narrow dynamic range it is possible to produce up to 64 perceptible gray levels, but one usually encounters less than 32 in practice. Hence, it is often desirable to compress the dynamic range of the acquired signal as early as possible in a way that best preserves the reflectance boundaries and topology of the scene while suppressing the temporal and spatial variations in the scene illumination. To this end, we combine image gathering with dynamic-range compression, similarly to the retinal processing in human vision.

In Sec. 2, we present a mathematical model of the visual communication system together with the criteria that we use to assess its performance quantitatively. This assessment is mathematically limited to a linear (small signal) analysis; however, as we show later (in Sec. 4), the linear optimization has a significant effect on the performance when nonlinear transformation is added. Next, in Sec. 3, we characterize the electro-optical design of image-gathering devices. This includes the human eye and recent developments of retina-like analog VLSI processors such as Mead's "silicon retina."²⁰ The comparison of the informationally optimized electro-optical design with the early stages in human vision is ob-

viously of interest because these stages are constrained by the same critical limiting factors as visual communication.²¹ Finally, in Sec. 4, we evaluate the performance of the visual communication channel as a function of the electro-optical design and the dynamic range compression, considering both image reconstruction and restoration. The difference between these two image representations is important: whereas *reconstruction* is concerned with producing a continuous representation of the digital *output* of the image-gathering device, *restoration* is concerned with producing a representation of the *input* to this device.

2 Mathematical Model

2.1 Visual Communication Channel

Figure 1 depicts a model of the visual communication channel that combines image gathering and display, respectively, with digital encoding and restoration. Mathematical assessments of this model by communication theory are constrained by the assumptions that all processes are linear and isoplanatic, and that the radiance field and photosensor noise amplitudes are Gaussian, wide-sense stationary, and statistically independent.

Image gathering transforms the continuous radiance field $L(x,y)$ into the digital signal

$$s(x,y) = [KL(x,y) * \tau(x,y)] \downarrow\downarrow (x,y) + n_p(x,y) + n_q(x,y) \quad (1a)$$

where K is the steady-state gain of the linear radiance-to-signal conversion, $\tau(x,y)$ is the spatial response of the image-gathering device, and $n_p(x,y)$ and $n_q(x,y)$ are the additive, discrete photosensor and quantization noise, respectively. The symbol $*$ denotes convolution, and the function

$$\downarrow\downarrow (x,y) = XY \sum_{m=-\infty}^{\infty} \sum_{n=-\infty}^{\infty} \delta(x - Xm, y - Yn)$$

denotes sampling in the (x,y) rectangular coordinate system of the image-gathering process with sampling intervals (X,Y) . This sampling lattice fixes the spatial scale at which the communication channel operates. The treatment of quantization as an additive noise can be justified by Roberts' method for converting quantization noise to random noise of the same rms value.^{6,21} This conversion establishes a mathematical and perceptual equivalence between random and quantization noise. The Fourier transform of this process is

$$\hat{s}(v,\omega) = [K\hat{L}(v,\omega)\hat{\tau}(v,\omega)] * \downarrow\downarrow(v,\omega) + \tilde{n}_p(v,\omega) + \tilde{n}_q(v,\omega) \quad (1b)$$

where $\hat{L}(v,\omega)$ is the continuous radiance-field transform, $\hat{\tau}(v,\omega)$ is the SFR of the image-gathering device, $\tilde{n}_p(v,\omega)$ and $\tilde{n}_q(v,\omega)$ are the discrete noise transforms, and (v,ω) are the spatial frequencies with units of cycles per sample. The function

$$\downarrow\downarrow(v,\omega) = \sum_{m=-\infty}^{\infty} \sum_{n=-\infty}^{\infty} \delta\left(v - \frac{m}{X}, \omega - \frac{n}{Y}\right) = \delta(v,\omega) + \downarrow\downarrow_s(v,\omega)$$

is the Fourier transform of the sampling lattice, where $\delta(v,\omega)$

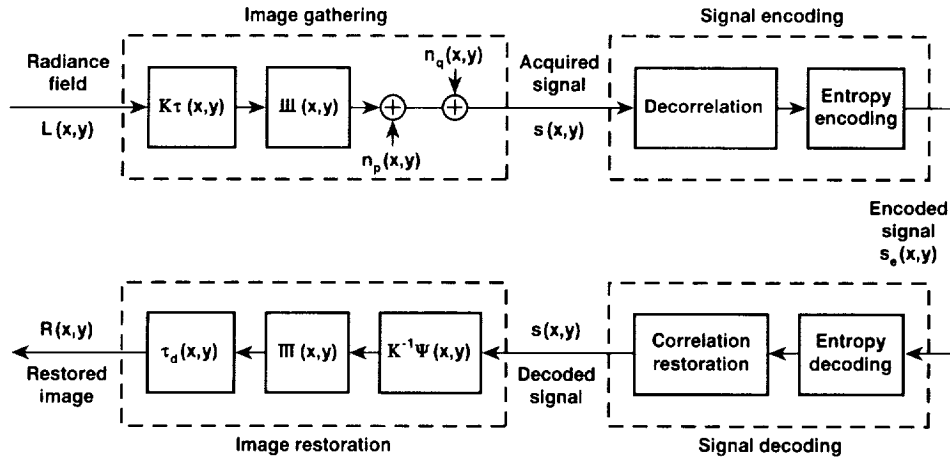


Fig. 1 Model of the visual communication channel.

is the Dirac delta function and $\hat{\Pi}(v, \omega)$ represents the sampling sidebands. The associated sampling passband

$$\hat{B} = \left[(v, \omega), |v| < \frac{1}{2X}, |\omega| < \frac{1}{2Y} \right]$$

has area $|\hat{B}| = 1/XY$.

The analog-to-digital conversion is done with κ levels for η -bit quantization, where $\eta = \log_2 \kappa$. This conversion is subject to the assumptions that the quantization is uniform, the error of any one sample is uncorrelated with that of any other sample, and the signal is equally likely to occur anywhere in the quantization interval $-c\sigma_s/\kappa$ to $c\sigma_s/\kappa$. The two parameters that define this interval are the variance σ_s^2 of the acquired signal given by (disregarding the photosensor noise)

$$\sigma_s^2 = \int \int_{-\infty}^{\infty} \hat{\Phi}_L(v, \omega) |\hat{\tau}(v, \omega)|^2 dv d\omega$$

and the constant c that adjusts the intervals of the quantization. Consequently, the acquired signal is quantized over the dynamic range of $-c\sigma_s/\kappa$ to $c\sigma_s/\kappa$, and signal values outside this range are assigned to either 0 or $\kappa - 1$. We let $c = \sqrt{3}$, for which the dynamic range encompasses 92% of the signal. This value of c relates information to data so that the theoretically highest information efficiency (as given in Section 2.2) is normalized to unity.^{16,17} Finally, it is convenient to assume that the photosensor noise has a white power spectral density (PSD) with variance σ_p^2 .

Restoration readjusts the magnitude of each sample of the digital signal $s(x, y)$, interpolates between the samples, and transforms the digitally processed signal into the continuous image $R(x, y)$, which has the Fourier transform $\hat{R}(v, \omega) = K^{-1} \hat{s}(v, \omega) \hat{\Psi}(v, \omega)$. The Wiener filter $\hat{\Psi}(v, \omega)$, which minimizes the mean squared restoration error (MSRE) between $\hat{L}(v, \omega)$ and $\hat{R}(v, \omega)$, can be expressed as¹⁶⁻¹⁸

$$\hat{\Psi}(v, \omega) = \frac{\hat{\Phi}'_L(v, \omega) \hat{\tau}^*(v, \omega)}{\hat{\Phi}'_L(v, \omega) |\hat{\tau}(v, \omega)|^2 * \hat{\Pi}(v, \omega) + (K\sigma_L/\sigma_p)^{-2} + (K\sigma_L/\sigma_s)^{-2} \kappa^{-2}} \quad (2)$$

where $\hat{\Phi}'_L(v, \omega) = \sigma_L^{-2} \hat{\Phi}_L(v, \omega)$ is the normalized PSD of the radiance field with variance σ_L^2 , $K\sigma_L/\sigma_p$ is the rms signal-to-noise ratio (SNR) at the photo-sensor output, and $(K\sigma_L/\sigma_s)\kappa$ is the corresponding SNR for the quantization. As implemented here, this filter suppresses the blurring and raster effects of the image display process by interpolating between the acquired samples with a display lattice that is four times denser than the sampling lattice. This interpolation is depicted in Fig. 1 by the symbol $\hat{\Pi}(x, y)$. A denser image display lattice does not perceptibly improve the visual quality of the restored image, whereas a coarser lattice does reduce the visual quality. Reference 22 presents a filter that minimizes these reductions in visual quality even if, in addition to a coarser lattice, the computational support is constrained to further reduce the complexity of processing.

The PSD $\hat{\Phi}_L(v, \omega)$ of the radiance field $L(x, y)$ within an isoplanatism patch A is assumed to be²³⁻²⁵

$$\hat{\Phi}_L(v, \omega) = \frac{2\pi\mu^2\sigma_L^2}{[1 + (2\pi\mu\rho)^2]^{3/2}}, \quad (3)$$

where $\rho^2 = v^2 + \omega^2$ (Fig. 2). Figure 3(a) shows a target of random polygons that has this PSD. The target is generated by a Poisson process with mean distance μ (measured in sampling intervals) between radiance-field transitions and by an independent Gaussian intensity distribution with variance σ_L^2 at the transitions.²⁶ The mean distance μ between the edges of the polygons is treated as the mean spatial detail of the radiance field. That is, when $X = Y = \mu$, the scale of the sampling lattice coincides with the mean spatial detail. Figure 3(b) shows a target of resolution wedges that we include to facilitate assessments of the fidelity with which fine detail near the sampling lattice can be restored.

2.2 Performance Criteria

Information theory treats the restored image $R(x, y)$ as a received message that gives information about the radiance field $L(x, y)$ and accounts for degradations as loss of information. In this sense, the information \mathcal{H} can be expressed as¹⁶⁻¹⁸

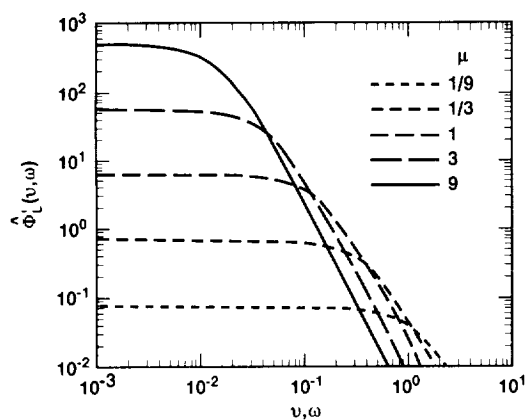


Fig. 2 Normalized PSD $\hat{\Phi}'_L(\nu, \omega)$ of the random radiance field with mean spatial detail μ relative to the sampling lattice.

$$\mathcal{H} = \frac{1}{2} \iint_{\hat{B}} \log_2 \left[1 + \frac{\hat{\Phi}'_L(\nu, \omega) |\hat{\tau}(\nu, \omega)|^2}{\hat{\Phi}'_L(\nu, \omega) |\hat{\tau}(\nu, \omega)|^2 * \iint_{\hat{B}} (\nu, \omega) + (K\sigma_L/\sigma_p)^{-2} + (K\sigma_L/\sigma_s)^{-2} \kappa^{-2}} \right] \times d\nu d\omega. \quad (4)$$

The information \mathcal{H} that the acquired signal contains, given here as the average per digital sample, is Shannon's rate of transmission of information, or information rate. \mathcal{H} reaches its theoretical upper bound

$$\mathcal{H}_m = \frac{1}{2} |\hat{B}| \log_2 [1 + (K\sigma_L/\sigma_p)^2] \quad (5)$$

when

$$\hat{\Phi}_L(\nu, \omega) = \begin{cases} \sigma_L^2, & (\nu, \omega) \in \hat{B}, \\ 0, & \text{elsewhere,} \end{cases}$$

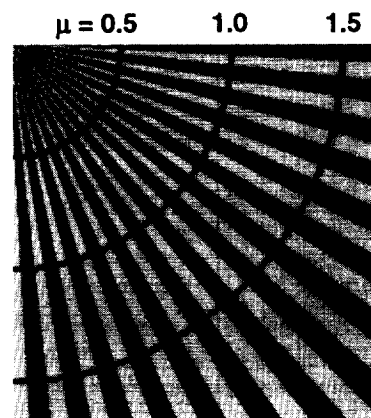
$$\hat{\tau}(\nu, \omega) = \begin{cases} 1, & (\nu, \omega) \in \hat{B}, \\ 0, & \text{elsewhere,} \end{cases}$$

and the quantization noise is negligible. This upper bound is Shannon's channel capacity, which is constrained only by the bandwidth \hat{B} and SNR $K\sigma_L/\sigma_p$. However, the image-gathering process inevitably bars \mathcal{H} from reaching \mathcal{H}_m , because \mathcal{H} is constrained also by the PSDs $\hat{\Phi}_L(\nu, \omega)$ of natural radiance fields and by the realizable SFRs $\hat{\tau}(\nu, \omega)$ of optical apertures, both of which decrease smoothly with increasing spatial frequency.

The information \mathcal{H} for visual communication reaches its maximum value when the sampling passband \hat{B} best matches the radiance-field PSD $\hat{\Phi}_L(\nu, \omega)$. We designate this maximum value as the information capacity \mathcal{H}_c . Ordinarily, it occurs when the sampling interval is near the mean spatial detail μ . Comparisons of the information capacity \mathcal{H}_c with Shannon's channel capacity \mathcal{H}_m reveal that the image-gathering process constrains \mathcal{H}_c to about half of \mathcal{H}_m .^{16,17}



(a)



(b)

Fig. 3 Targets: (a) random polygons with mean distance $\mu = 3$ per sample and (b) resolution wedges.

The theoretical minimum data rate \mathcal{E} associated with the information \mathcal{H} is given by the mutual information between the acquired signal before quantization and its quantized representation.¹³ It can be expressed as¹⁸

$$\mathcal{E} = \frac{1}{2} \iint_{\hat{B}} \log_2 \left[1 + \frac{\hat{\Phi}'_L(\nu, \omega) |\hat{\tau}(\nu, \omega)|^2 * \iint_{\hat{B}} (\nu, \omega) + (K\sigma_L/\sigma_p)^{-2}}{(K\sigma_L/\sigma_s)^{-2} \kappa^{-2}} \right] d\nu d\omega. \quad (6)$$

This expression for \mathcal{E} represents the entropy of completely decorrelated data. It sets the theoretical lower bound on the data rate that can be attained with lossless encoding. To distinguish entropy from information, we measure entropy in binary units (bits), as is common for data, and information in binary information units (bifs).

Note that the sampling sidebands (aliasing) and photo-sensor noise, which reduce \mathcal{H} in Eq. (4), increase \mathcal{E} in Eq. (6). Hence, \mathcal{E} approaches its lower limit \mathcal{H} only when these distortions are masked by coarse quantization. About 80% to 90% decorrelation is obtained when either differential pulse code modulation (DPCM) or critically sampled mul-

iresolution decomposition is combined with Huffman encoding.¹⁸ The decomposition does not improve on the de-correlation produced by the computationally much simpler DPCM.

It is intuitively attractive to characterize the information efficiency of the image-gathering process by the ratio \mathcal{H}/\mathcal{E} and to adjust this ratio so that its theoretical upper bound is unity. This adjustment occurs naturally for the conditions of the PSD $\hat{\Phi}_L(\nu, \omega)$ and the SFR $\hat{\tau}(\nu, \omega)$ that lead from \mathcal{H} given by Eq. (4) to its upper bound \mathcal{H}_m given by Eq. (5). These conditions are implicitly included in Eq. (2) for $\hat{\Psi}(\nu, \omega)$, Eq. (4) for \mathcal{H} , and Eq. (6) for \mathcal{E} . An important result of earlier assessments,¹⁶⁻¹⁸ which we also show here, is that the electro-optical design that maximizes the information capacity \mathcal{H}_c for a given SNR $K\sigma_L/\sigma_p$ also maximizes the information efficiency $\mathcal{H}_c/\mathcal{E}$. But there always remains a trade-off, for each design, between \mathcal{H}_c and $\mathcal{H}_c/\mathcal{E}$ in the selection of the number of quantization levels.

The fidelity F is a measure of the similarity between the radiance field $L(x, y)$ and the image $R(x, y)$ as defined by^{27,28}

$$F = 1 - \frac{\iint_A |L(x, y) - R(x, y)|^2 dx dy}{\iint_A |L(x, y)|^2 dx dy} \quad (7)$$

The maximum value of F for the image $R(x, y)$ restored by the Wiener filter $\hat{\Psi}(\nu, \omega)$ is^{16,17}

$$\begin{aligned} \mathcal{F} &= \iint_{-\infty}^{\infty} \hat{\Phi}'_L(\nu, \omega) \hat{\tau}(\nu, \omega) \hat{\Psi}(\nu, \omega) d\nu d\omega \\ &= \iint_{-\infty}^{\infty} \hat{\Phi}'_L(\nu, \omega) (1 - 2^{-\mathcal{H}(\nu, \omega)}) d\nu d\omega, \end{aligned} \quad (8)$$

where $\mathcal{H}(\nu, \omega)$ is the spectral information density given by the integrand of Eq. (4). Another important result of earlier assessments,^{16,17} which we also show here, is suggested by the dependence of \mathcal{F} on $\mathcal{H}(\nu, \omega)$; namely, that the image-gathering device that is designed to maximize the information capacity \mathcal{H}_c ordinarily can be relied on to maximize the fidelity of the Wiener restoration. The apparent lack of resolution and sharpness of Wiener restorations is not, as was long believed, a shortcoming of the fidelity criterion.^{16,17} Instead, it is the failure of the traditional formulation of the Wiener filter, like that of other restoration filters published in the prevalent digital image-processing literature,⁷⁻¹² to allow fully for image gathering and display. When the Wiener

filter fully includes these processes, then it produces images with improved resolution and sharpness as well as fidelity. Spatial details as small as the sampling interval are usually resolved. However, these images are also more sensitive to visual defects such as aliasing artifacts and photosensor noise. These defects diminish and the visual quality of Wiener restorations improves in clarity with increasing information, even after the maximum fidelity has essentially been reached, until this improvement is gradually ended by the unavoidable compromise among resolution, sharpness, aliasing artifacts, and ringing. The visual quality may often be enhanced at a small loss in resolution and sharpness by combining the Wiener filter with a modest amount of smoothing.¹⁶⁻¹⁸

3 Electro-optical Design

3.1 Design Parameters

Image-gathering devices are commonly specified by their IFOV and SNR. (To avoid possible confusion, it should be pointed out here that the SNR is given elsewhere more commonly for the average rather than for the rms signal value.) These specifications can be injected into the image-gathering model given by Eqs. (1) via the steady-state gain (in amperes)^{1,2}

$$K = k A \Omega \int_0^\infty L(\lambda) r(\lambda) d\lambda \approx \frac{\pi k \gamma^2}{4 F^2} \int_0^\infty L(\lambda) r(\lambda) d\lambda \quad (9)$$

where $A = \pi D^2/4$ is the area of the objective lens aperture, $\Omega = (\gamma/f_p)^2 \approx (\gamma/f)^2$ steradians (sr) is the solid angle of the IFOV, and $F = f/D$ is the lens f number. Other design parameters are identified in Fig. 4 and Table 1. The SFR $\hat{\tau}(\nu, \omega)$ of the image-gathering device is the product of the SFR $\hat{\tau}_l(\nu, \omega)$ and $\hat{\tau}_p(\nu, \omega)$ of the objective lens and photosensor aperture, respectively; i.e.,

$$\hat{\tau}(\nu, \omega) = \hat{\tau}_l(\nu, \omega) \hat{\tau}_p(\nu, \omega) \quad (10)$$

The objective lens is characterized in Sec. 3.2 by its diffraction-limited performance. However, few real lenses achieve this performance over their whole field.^{29,30} The photosensor array is characterized in Sec. 3.3 for the square and hexagonal sampling lattices, and lateral inhibition with these two arrays is characterized in Sec. 3.4. It is common, as we do here, to characterize the objective lens by its coherent cutoff frequency $1/2\lambda F$ and the optical geometry that the

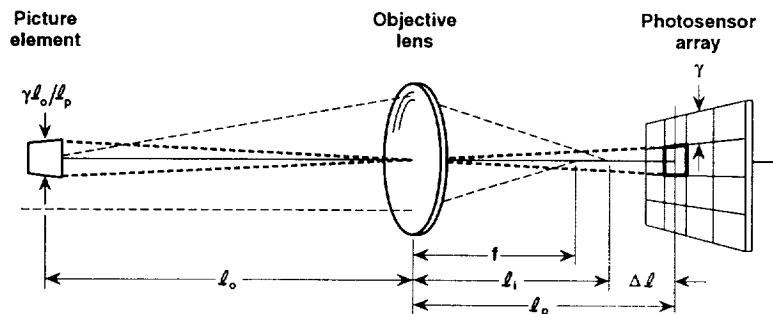


Fig. 4 Optical configuration of the image-gathering device with photosensor array.

Table 1 Design parameters.

Parameter	Symbol	Unit
Lens aperture diameter	D	m
Lens focal length	f	m
Photosensor aperture spacing	X	m
Photosensor aperture width	γ	m
Photosensor distance from lens	ℓ_p	m
Wavelength	λ	μm
Photosensor responsivity	$r(\lambda)$	A/W
Spectral radiance	$L(\lambda)$	$Wm^{-2}sr^{-1}\mu m^{-1}$

objective lens forms with the photosensor aperture by the optical design index $\gamma/2\lambda F$.

3.2 Objective Lens

The SFR, or normalized optical transfer function (OTF), $\hat{\tau}_t(v, \omega)$ of a diffraction-limited lens with a circular aperture is³¹⁻³³

$$\hat{\tau}_t(v, \omega) = \frac{\iint_{-\infty}^{\infty} P_t(\bar{v}' + \bar{\rho}/2, \bar{\omega}') P_t^*(\bar{v}' - \bar{\rho}/2, \bar{\omega}') \exp(iu\bar{\rho}\bar{v}') d\bar{v}', d\bar{\omega}'}{\iint_{-\infty}^{\infty} P_t(\bar{v}', \bar{\omega}') P_t^*(\bar{v}', \bar{\omega}') d\bar{v}' d\bar{\omega}'} \quad (11)$$

where

$$P_t(\bar{v}, \bar{\omega}) = \begin{cases} t(\bar{v}, \bar{\omega}), & \bar{v}^2 + \bar{\omega}^2 \leq 1 \\ 0 & \text{elsewhere,} \end{cases}$$

$$\bar{\rho} = (v^2 + \omega^2)^{1/2} 2\lambda F,$$

and $t(\bar{v}, \bar{\omega})$ is the transmittance. The dimensionless spatial-frequency variables \bar{v} , $\bar{\omega}$, and $\bar{\rho}$ are normalized to the coherent cutoff frequency $1/2\lambda F$. The defocus parameter u is

$$u \approx \frac{\pi}{2\lambda} \Delta \ell \left(\frac{D}{\ell_i} \right)^2 \approx \frac{\pi}{2\lambda F^2} \Delta \ell,$$

where $\Delta \ell = |\ell_i - \ell_p|$, and ℓ_i is the image-plane distance from the lens (Fig. 4).

Hopkins³¹⁻³³ has formulated the SFR of a defocused diffraction-limited lens with a clear aperture, i.e., $t(\bar{v}, \bar{\omega}) = 1$, and Mino and Okano³⁴ have extended this formulation to include

two circularly symmetric variable lens transmittance shadings that reduce defocus blur. OTFs for different shadings also can be obtained directly by numerical integration of Eq. (11).³⁵ Figure 5 shows the SFR $\hat{\tau}_t(v, \omega)$ for a clear and two shaded apertures. The shadings are given by

$$t(\bar{v}, \bar{\omega}) = 1 - \bar{\rho}^\beta \quad (12)$$

with $\beta = 1$ and 2. The ratio k of light transmitted through the shaded aperture to a clear aperture, i.e., the effective transmittance in Eq. (9), is

$$k = 2 \int_0^1 \bar{\rho} |t(\bar{\rho})|^2 d\bar{\rho}. \quad (13)$$

As can be seen, the shading reduces the effect of defocus on the SFR of the objective lens. However, this improvement can be gained only at a loss of transmittance.

The angular sensitivity of the eye's photoreceptors (i.e., the Stiles-Crawford effect³⁶) produces a similar result to the variable lens transmittance shading. Metcalf³⁷ has shown that the angular sensitivity of the photoreceptors can be considered as equivalent to a variable pupil aperture transmittance, and Carroll³⁸ has shown that this variable transmittance produces a SFR that is similar to the one given by Fig. 5(b) for $\beta = 2$. However, the advantages of this angular sensitivity, or its equivalent aperture shading, have apparently not been widely recognized; namely, that it enhances the SFR within the photoreceptor sampling passband and renders the SFR less sensitive to defocus.

3.3 Photosensor Arrays

Figure 6 depicts two photosensor arrays characterized by $\tau_p(x, y) \lll(x, y)$ and $\hat{\tau}_p(v, \omega) \ast \lll(v, \omega)$. For the conventional square array³⁵

$$\tau_p(x, y) = \begin{cases} 1/\gamma^2, & |x| < \gamma/2, \quad |y| < \gamma/2 \\ 0 & \text{elsewhere,} \end{cases} \quad (14a)$$

$$\hat{\tau}_p(v, \omega) = \text{sinc } \gamma v \text{ sinc } \gamma \omega, \quad (14b)$$

$$\lll(x, y) = X^2 \sum_{m=-\infty}^{\infty} \sum_{n=-\infty}^{\infty} \delta(x - Xm, y - Yn), \quad (15a)$$

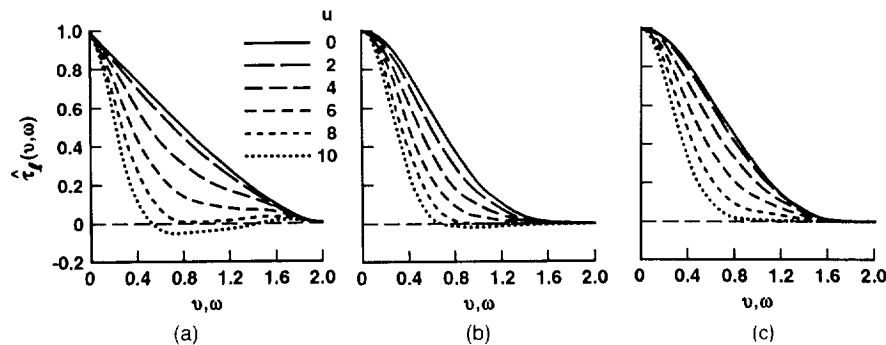


Fig. 5 SFRs of diffraction-limited lens with clear and shaded apertures for a coherent cutoff frequency $1/2\lambda F = 1$ and several values of the defocus u : (a) clear aperture, $k = 1$, (b) shaded aperture, $\beta = 2$ and $k = 0.33$, and (c) shaded aperture, $\beta = 1$ and $k = 0.17$.

$$\hat{\Pi}(v, \omega) = \sum_{m=-\infty}^{\infty} \sum_{n=-\infty}^{\infty} \delta\left(v - \frac{m}{X}, \omega - \frac{n}{X}\right), \quad (15b)$$

and for the regular hexagonal array³⁵

$$\tau'_p(x, y) = \begin{cases} \frac{2}{\sqrt{3}\gamma'^2}, & |y| < \frac{\gamma'}{2}, \quad \frac{\sqrt{3}}{2}|x| + \frac{1}{2}|y| < \frac{\gamma'}{2}, \\ 0 & \text{elsewhere,} \end{cases} \quad (16a)$$

$$\begin{aligned} \hat{\tau}'_p(v, \omega) = & \frac{1}{3} \left\{ \text{sinc}\left(\frac{\gamma'v}{\sqrt{3}}\right) \left[\cos\frac{\pi}{2}\gamma'\left(\frac{v}{\sqrt{3}} - \omega\right) \right. \right. \\ & \times \text{sinc}\frac{1}{2}\gamma'\left(\frac{v}{\sqrt{3}} + \omega\right) \\ & + \cos\frac{\pi}{2}\gamma'\left(\frac{v}{\sqrt{3}} + \omega\right) \text{sinc}\frac{1}{2}\gamma'\left(\frac{v}{\sqrt{3}} - \omega\right) \Big] \\ & + \cos\left(\frac{\pi\gamma'v}{\sqrt{3}}\right) \\ & \left. \times \text{sinc}\frac{1}{2}\gamma'\left(\frac{v}{\sqrt{3}} - \omega\right) \text{sinc}\frac{1}{2}\gamma'\left(\frac{v}{\sqrt{3}} + \omega\right) \right\}, \end{aligned} \quad (16b)$$

$$\begin{aligned} \hat{\Pi}'(x, y) = & \frac{\sqrt{3}}{2} X'^2 \sum_{m=-\infty}^{\infty} \sum_{n=-\infty}^{\infty} \\ & \times \delta\left(x - \frac{\sqrt{3}}{2} X'(m+n), y - \frac{1}{2} X'(m-n)\right). \end{aligned} \quad (17a)$$

$$\hat{\Pi}'(v, \omega) = \sum_{m=-\infty}^{\infty} \sum_{n=-\infty}^{\infty} \delta\left(v - \frac{(m+n)}{\sqrt{3}X'}, \omega - \frac{(m-n)}{X'}\right). \quad (17b)$$

The sampling passband

$$\hat{B} = \left\{ (v, \omega); |v| < \frac{1}{2X}, |\omega| < \frac{1}{2X} \right\}$$

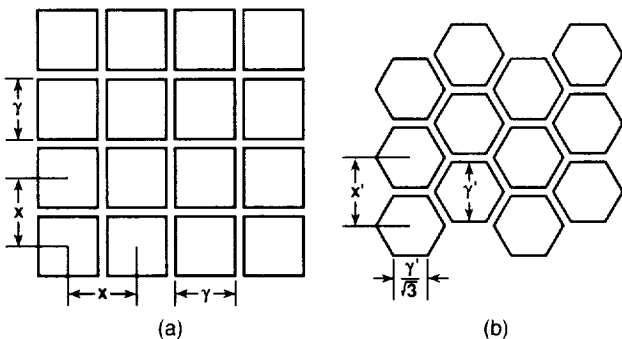


Fig. 6 Photocensor arrays: (a) square and (b) hexagonal.

of the square lattice has area $|\hat{B}| = 1/X^2$, and the sampling passband

$$\hat{B}' = \left\{ (v, \omega); |v| < \frac{1}{\sqrt{3}X'}, \frac{|v|}{2} + \frac{\sqrt{3}|\omega|}{2} < \frac{1}{\sqrt{3}X'} \right\}$$

of the hexagonal lattice has area $|\hat{B}'| = 2/\sqrt{3}X'^2$. The areas $|\hat{B}|$ and $|\hat{B}'|$, and hence the sampling densities of the square and hexagonal lattices, are equal to each other when the dimensions X and X' are such that $X = (\sqrt{3}/2)^{1/2} X' = 0.93X'$.

Past comparisons of the square and hexagonal lattice have been based on the premise that the signal spectrum is circularly symmetric and bandlimited.^{39,40} Given this premise, it has been shown that the hexagonal lattice optimizes the density with which the circularly symmetric sidebands can be arranged in the spatial-frequency domain without overlap, permitting exact reconstruction of the signal with a minimum number of samples. In particular, Peterson and Middleton³⁹ have shown that the contiguous sampling sidebands cover 90.8% of the spatial-frequency domain for the hexagonal lattice, compared with only 78.5% for the square lattice. Consequently, as Mersereau⁴⁰ has shown, the hexagonal lattice can have 13% fewer photosensors (and correspondingly larger photosensor areas) than the square lattice for the exact reconstruction of circularly symmetric, sufficiently sampled signals.

3.4 Lateral Inhibition

Figure 7 depicts a hypothetical mechanism that adds lateral inhibition to the two photocensor arrays. The diagram shows only those interconnections that form a single neighborhood subtraction. The subtraction is performed with either eight neighboring photosensors for the square array or six for the hexagonal array. For digital VLSI implementation, many more interconnections are required so that each photosensor, in effect, serves once in the central position and either eight or six times in the neighboring positions. However, for analog

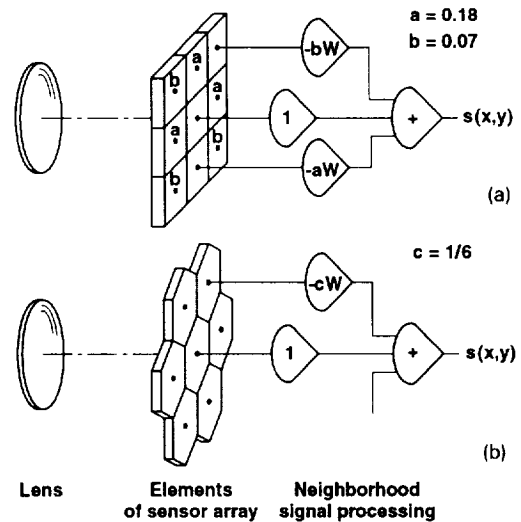


Fig. 7 Photocensor arrays with lateral inhibition: (a) square and (b) hexagonal.

VLSI implementations, this circuit can be implemented with a relatively simple resistive network.²⁰

For the square array, the spatial response becomes⁴¹

$$\begin{aligned} \tau_{pi}(x,y) = A(\zeta) & \left\{ \tau_p \left(\frac{x}{X}, \frac{y}{Y} \right) + a\zeta \left[\tau_p \left(\frac{x}{3X}, \frac{y}{Y} \right) \right. \right. \\ & + \tau_p \left(\frac{x}{X}, \frac{y}{3Y} \right) - 2\tau_p \left(\frac{x}{3X}, \frac{y}{Y} \right) \\ & + b\zeta \left[\tau_p \left(\frac{x}{3X}, \frac{y}{3Y} \right) - \tau_p \left(\frac{x}{3X}, \frac{y}{Y} \right) \right. \\ & \left. \left. - \tau_p \left(\frac{x}{X}, \frac{y}{3Y} \right) + \tau_p \left(\frac{x}{X}, \frac{y}{Y} \right) \right] \right\}, \end{aligned} \quad (18a)$$

where ζ ($0 \leq \zeta \leq 1$) is the lateral inhibition index and $\tau_p(x,y)$ is given by Eq. (14a). The corresponding SFR is

$$\begin{aligned} \hat{\tau}_{pi}(v,\omega) = A(\zeta) \hat{\tau}_p(v,\omega) & [1 - 4a\zeta(1 - \cos^2 \pi Xv - \cos^2 \pi X\omega) \\ & + 4b\zeta(1 - 2 \cos^2 \pi Xv)(1 - 2 \cos^2 \pi X\omega)], \end{aligned} \quad (18b)$$

where $\hat{\tau}_p(v,\omega)$ is given by Eq. (14b). Only the form of $\hat{\tau}_{pi}(v,\omega)$ should be used to characterize the SFR of the photosensor array with lateral inhibition. The factor $A(\zeta)$ must be associated with the photosensor and aliased noise because⁴¹ the normalization of $\hat{\tau}_{pi}(v,\omega)$ is intimately tied to the gain constant K . The SFR $\hat{\tau}_{pi}(v,\omega)$ most closely approaches circular symmetry when $a=0.18$ and $b=0.07$.

If electronic noise sources other than the photosensor are disregarded, then the output noise level is

$$\sigma_{pi} = |A(\zeta)| \left[1 + \left(\frac{a}{2} + \frac{b}{2} \right) \zeta^2 \right]^{1/2} \sigma_p.$$

Both the signal power and the aliased noise power are proportional to $|A(\zeta)|^2$. Therefore, the gain $|A(\zeta)|$ in the SNR expression $K\sigma_L/\sigma_p$ cancels, and one may choose any normalization factor $A(\zeta)$ as long as the noise σ_p is replaced by the σ_{pi} . Here we let $A(\zeta)=1$. Hence, the increase in noise that lateral inhibition causes for this hypothetical circuit is at most a factor of 1.13 when $\zeta=1$.

Similarly, for the hexagonal array, the spatial response becomes⁴¹

$$\begin{aligned} \tau'_{pi}(x,y) = A(\zeta) & \left[\tau'_p(x,y) - \frac{\zeta}{6} \sum_{\substack{m,n=-1 \\ (m \neq n)}}^{+1} \right. \\ & \left. \tau'_p \left(x - \frac{\sqrt{3}}{2} X'(m+n), y - \frac{X'}{2} (m-n) \right) \right], \quad \gamma = X, \end{aligned} \quad (19a)$$

where $\tau'_p(x,y)$ is given by Eq. (16a). The corresponding SFR is

$$\hat{\tau}'_{pi}(v,\omega) = A(\zeta) \hat{\tau}'_p(v,\omega) \left(1 - \frac{\zeta}{6} [2 \cos(2\pi X'\omega) \right.$$

$$\left. + 2 \cos \pi X'(\sqrt{3}v + \omega) + 2 \cos \pi X'(\sqrt{3}v - \omega) \right], \quad (19b)$$

where $\hat{\tau}'_p(v,\omega)$ is given by Eq. (18a). The noise σ_p is now replaced by

$$\sigma_{pi} = |A(\zeta)| (1 + \zeta^2/6)^{1/2} \sigma_p,$$

which for $A(\zeta)=1$ is at most a factor of 1.17 when $\zeta=1$.

3.5 Information Capacity

Figures 8 and 9 characterize the information capacity \mathcal{H}_c as a function of the optical design index $\gamma/2\lambda F$ for several SNRs $K\sigma_L/\sigma_N$. The noise variance σ_N^2 includes both photosensor and quantization noise. The objective lens is clear in Fig. 8 and shaded in Fig. 9. Both figures provide for the square and hexagonal photosensor array lattices, either without lateral inhibition ($\zeta=0$) or with maximum lateral inhibition ($\zeta=1$).

The curves show that \mathcal{H}_c depends critically on the optical design index $\gamma/2\lambda F$. The information capacity is irrevocably constrained to be $\mathcal{H}_c < 3$ bifs, regardless of the SNR, however high it may be, if the optical design index for a diffraction-limited objective lens falls outside the range $0.3 < \gamma/2\lambda F < 0.6$. Within this range, the information capacity reaches its maximum value for the SNR $K\sigma_L/\sigma_N = 256$ when $\gamma/2\lambda F \approx 0.35$ for the clear lens and when $\gamma/2\lambda F \approx 0.4$ for the shaded lens. Then, $\mathcal{H}_c \approx 5$ bifs without lateral inhibition and $\mathcal{H}_c \approx 4.5$ bifs with maximum lateral inhibition. \mathcal{H}_c is a little lower than these values for the clear aperture and square sampling lattice, and it is a little higher for the shaded aperture and hexagonal sampling lattice. However, \mathcal{H}_c depends far more on the optical-design index and the SNR than on the lens shading, sampling geometry, or lateral inhibition.

To characterize the dependence of \mathcal{H}_c on the electro-optical design in more detail, Figs. 10 and 11 illustrate the responses of the image-gathering device for the square and hexagonal arrays, respectively. As can be seen, the SFRs of the photodetection mechanism extend far beyond the sampling passband \hat{B} even for contiguous apertures. Therefore, to optimize the information capacity \mathcal{H}_c , the objective lens must suppress the out-of-band portion of the SFR. The exact amount of suppression becomes increasingly critical as one tries to improve \mathcal{H}_c by increasing $K\sigma_L/\sigma_N$.

Figure 12 shows that Gaussian responses closely approximate the SFRs $\hat{\tau}(v,\omega)$ of the image-gathering device. This allows us to model the SFR of image gathering with lateral inhibition by the difference-of-Gaussians (DOG) function

$$\hat{\tau}(v,\omega;\xi,\zeta) = \exp \left[-(\rho/\xi)^2 \right] - \zeta \exp \left[-(1.6\rho/\xi)^2 \right], \quad (20)$$

where, as Fig. 13 depicts, ξ is the optical response index that controls the relationship between $\hat{\tau}(v,\omega;\xi,\zeta)$ and \hat{B} (i.e., the trade-off between aliasing and blurring), and ζ is the lateral-inhibition index that controls the dynamic-range compression. The DOG response for $\zeta=1$ closely approximates the Laplacian-of-Gaussian ($\nabla^2 G$) response, where $\nabla^2 = \partial^2/\partial x^2 + \partial^2/\partial y^2$ is the Laplacian operator. This operator, in effect,

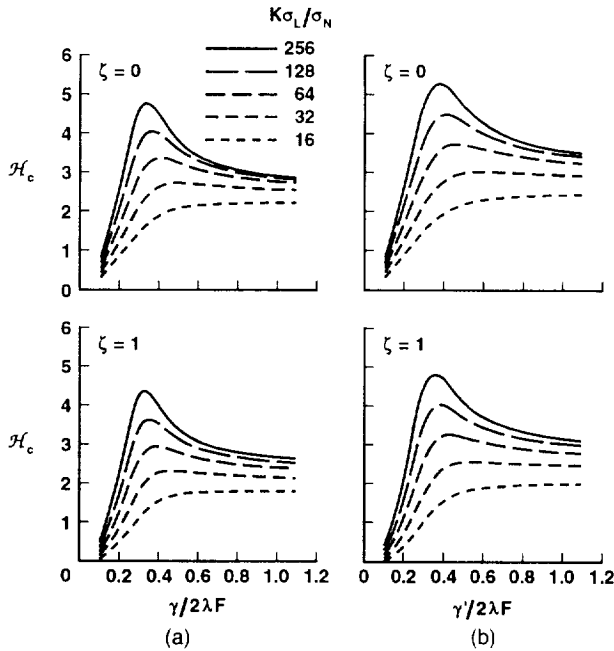


Fig. 8 Information capacity \mathcal{H}_c as a function of the optical-design index $\gamma/2\lambda F$ for several SNRs $K\sigma_L/\sigma_N$. The results are given for a clear objective lens and the (a) square and (b) hexagonal photosensor arrays with contiguous apertures. The lateral inhibition is either $\zeta = 0$ or 1.

enhances the radiance-field transitions after those transitions have been smoothed by the (approximately) Gaussian response of the image-gathering device.

3.6 Human Vision

Early vision is constrained by the same critical limiting factors as visual communication. The resolving power (or sampling passband) of all eyes, in invertebrates as well as in vertebrates, appears to be limited by the difficulty of confining light within the outer segment of a photoreceptor.¹⁹ Center-to-center spacings of foveal cones less than $2\ \mu\text{m}$ have never been found, regardless of the size of the eye.⁴² Moreover, the pupil f number remains remarkably constant in a variety of species, ranging from humans to birds of prey of widely different sizes.⁴² The sensitivity of the eye appears to be limited by the thermal stability of the photosensitive pigments of the photoreceptors. Because "dark" noise is extremely low, equivalent to only a few quanta of light,¹⁹ the sensitivity essentially is limited by photon noise rather than the statistically independent noise assumed in this assessment.

The human eye as a whole can encompass the wide dynamic range of the natural radiance fields that one commonly encounters. If one allows for changes in pupil (or lens) diameter and for optical losses, then the dynamic range of the radiance incident on the retina reduces to $\sim 10^7 : 1$. Barlow¹⁹ estimates that the number of distinguishable intensity levels in this dynamic range is ≈ 200 . Retinal processing seems to reduce this number of levels by a factor of ≈ 5 to the upper limit of ≈ 40 levels that each nerve fiber can transmit from the retina to the visual cortex within $\approx 1/20$ s to avoid prolonging the reaction time.

The eye's pupil diameter is $D = 2.5$ mm in bright light, and the effective focal length is $f = 17$ mm (i.e., $F = 6.8$). The

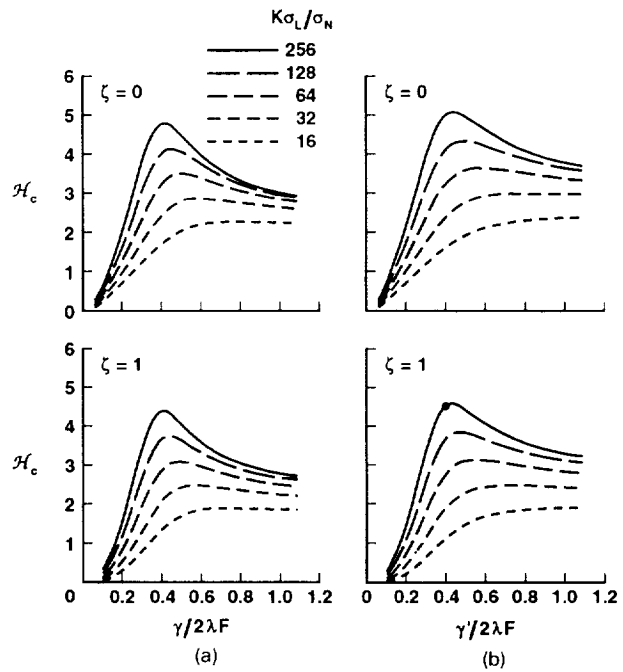


Fig. 9 Same as Fig. 8, but for a shaded objective lens with $\beta = 2$. The symbol \bullet marks the performance of the human eye.

photoreceptor spectral responsivity is centered around $\lambda = 0.56\ \mu\text{m}$, and the width of the contiguous foveal cones arranged in a hexagonal lattice is $\gamma' = 3\ \mu\text{m}$. Hence, the IFOV $\gamma'/f = 0.18\ \text{mrad} \approx 0.01\ \text{deg}$, and the optical design index $\gamma'/2\lambda F = 0.4$. Finally, the angular sensitivity of the eye's photoreceptors produces^{37,43} a similar effect to the lens aperture shading for $\beta = 2$.

The number of distinguishable levels, ι , can be related to the SNR $K\sigma_L/\sigma_N$ by⁴⁴

$$\iota = [1 + (K\sigma_L/\sigma_N)^2]^{1/2}. \quad (21)$$

According to this relationship, the $\iota = 200$ distinguishable levels are equivalent to a SNR of $K\sigma_L/\sigma_N = 256$ (for $\mu = 1$ and $\zeta = 0.3$).¹⁶ Hence, there exists an intuitively appealing correspondence between the design of the human eye and that of an image-gathering device that is informationally optimized, as characterized in Fig. 8(b) for $\gamma'/2\lambda F = 0.4$, $K\sigma_L/\sigma_N = 256$. It follows that the eye's information capacity is $\mathcal{H}_c \approx 4.5$ bifs (or 23 information levels). This performance is robust to changes in pupil diameter. As diffraction blur decreases with increasing diameter, aberrations increase.¹⁹ This compensation has not, to our knowledge, been exploited for digital cameras, even though it could improve their performance and occasionally also reduce the cost of their optics simply by relaxing constraints on aberrations.

If the DOG function given by Eq. (20) is used as a basis for modeling the angular response of the human eye, then its response for the optical design index $\gamma'/2\lambda F = 0.4$ is the one shown in Fig. 14. This DOG function is the best-known model of receptive fields and has been used successfully to model the spatial and spatial-frequency responses for individual neurons^{45,46} in both the retina and the lateral geniculate nucleus (LGN). Measurements of the highest-resolution pro-

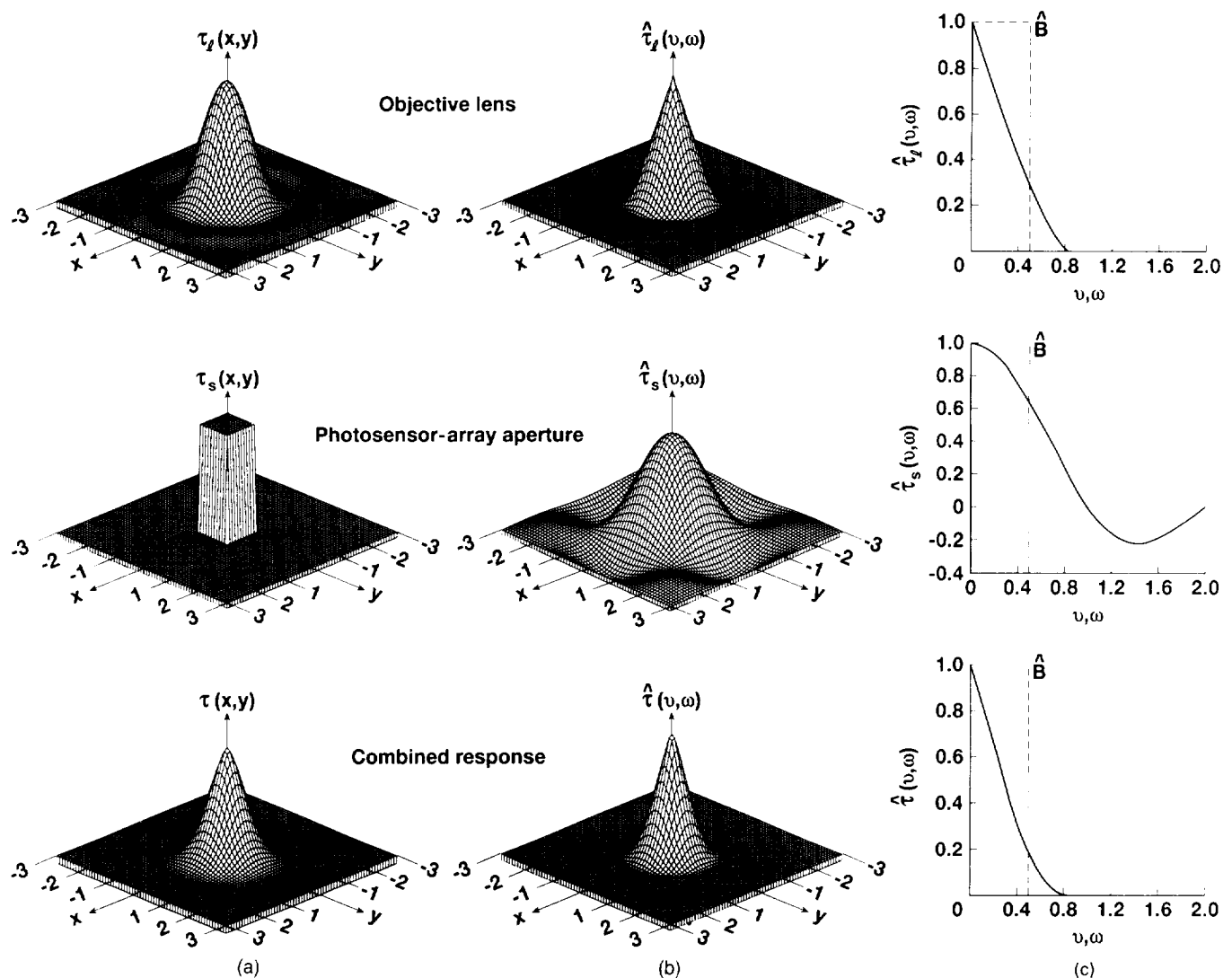


Fig. 10 Spatial responses and SFRs of the image-gathering device with the square photosensor array and the clear objective lens. The optical design index $\gamma/2\lambda F = 0.42$.

cessing in human vision have been limited to anatomical and perceptual data, neither of which can provide direct information about the angular response. The gap in physiological data is of necessity filled by other primate studies, especially of the macaque monkey, whose vision is considered to be similar to human vision. Moreover, these studies of neuron responses have emphasized the LGN, i.e., the target of the optic nerve tract from the retina rather than the retina itself. However, it seems reasonable to assume that the highest-resolution neurons in the retina, the midget ganglion cells, correspond directly to their counterparts, the parvocellular layers of the LGN, and that both of these are the neural structures responsible for the highest-spatial-resolution processing in human vision.

Anatomical measurements of neural structures in the retina indicate that the IFOV per cell is 0.023 deg,⁴⁷ which corresponds closely to the center diameter of the DOG model in Fig. 14(a). Physiological measurements of primate retinal responses are consistent with this center dimension, but differ

about the shape and extent of the surround response.⁴⁸ One type of surround resembles the DOG response based on nearest neighbors but has an additional positive annular response. The other type has a very wide weak surround about 30 times larger than the center. Of course, the surround response does not affect the finest detail that can be resolved, but rather deals with the lower spatial frequencies. It is, therefore, noteworthy that the second response, with the wide but weak surround, when coupled with a log intensity response, becomes a central element in several lightness theories.⁴⁹

Physiological measurements of contrast sensitivity and dynamic range at the highest resolution of processing have been largely confined to the LGN neurons. Most studies are consistent in finding that the contrast sensitivity for the parvo cells is only about 10 : 1 but covers a relatively large dynamic range.⁵⁰ Perceptual measurements indicate a contrast sensitivity that is even coarser at the highest spatial frequency, only about two shades of gray,⁵¹ but at lower spatial frequencies approaches 200 : 1. Recent measurements also sug-

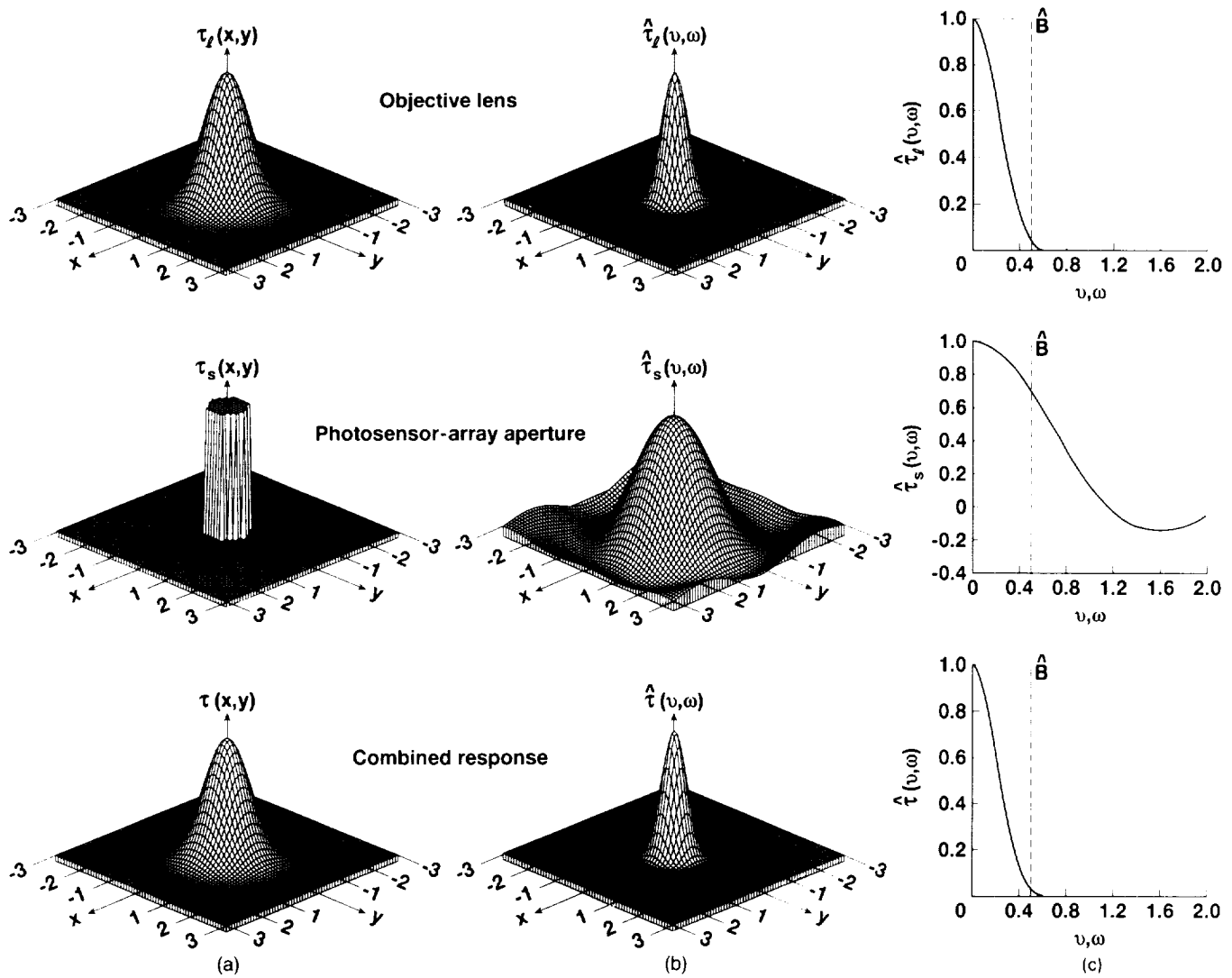


Fig. 11 Same as Fig. 10, but for the hexagonal photosensor array and the shaded objective lens with $\beta = 2$. The optical design index $\gamma' / 2\lambda F = 0.34$.

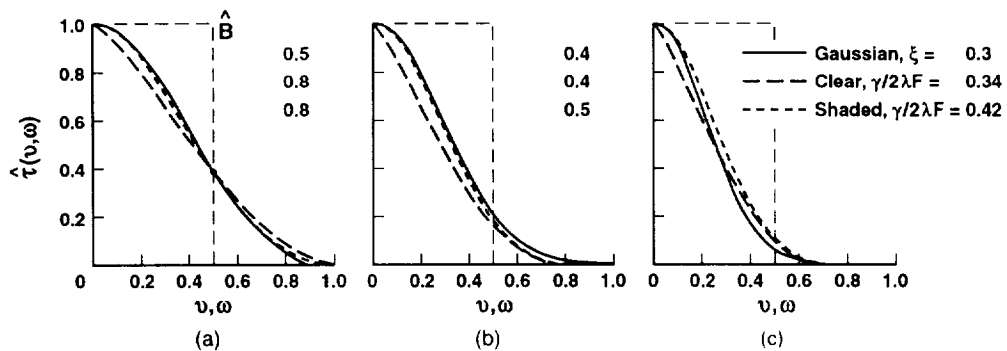


Fig. 12 Informationally optimized SFRs for three SNRs: (a) $K_{\tau_L}/\sigma_N = 16$, (b) $K_{\tau_L}/\sigma_N = 64$, (c) $K_{\tau_L}/\sigma_N = 256$. The SFRs are given for the clear and shaded ($\beta = 2$) objective lens and the square photosensor array with contiguous apertures ($\gamma = X = 1$). Also shown are Gaussian approximations of these SFRs.

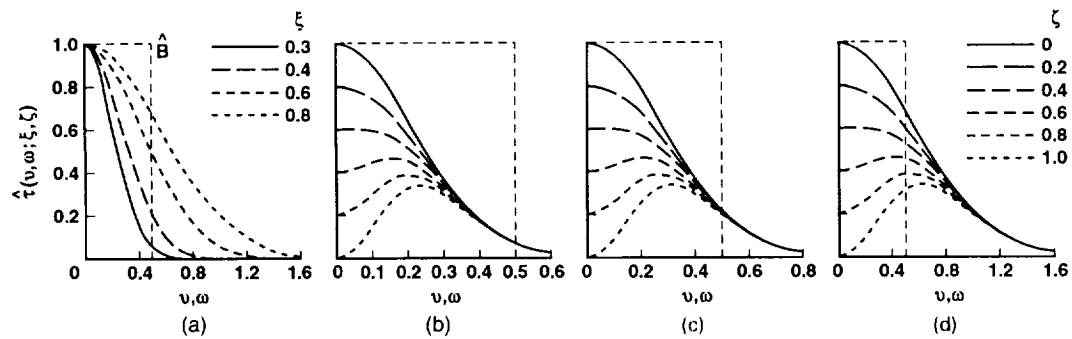


Fig. 13 Difference-of-Gaussians (DOG) SFRs for (a) $\xi=0$, (b) $\xi=0.3$, (c) $\xi=0.4$, and (d) $\xi=0.8$.

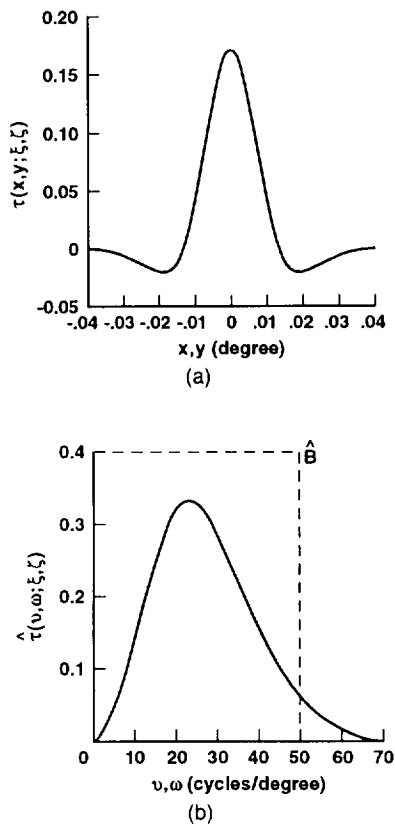


Fig. 14 DOG model of human visual response: (a) angular response in degrees, and (b) angular frequency response in cycles per degree.

gest a variety of nonlinear interactions in visual processing in addition to the log intensity response, which provides dynamic-range compression, adaptive contrast, and contextual sensitivity.^{52,53}

3.7 Analog and Digital VLSI

Focal-plane processing may be implemented in a number of different ways, if we take the term to mean processing within a camera but not necessarily within the image plane proper. Pure image-plane processing is realized in Mead's "silicon retina," where photosensor territory is sacrificed for processing territory with an analog VLSI resistive network.²⁰

This disadvantage can be overcome by moving the analog processing to a separate chip.⁵⁴ This move allows the photosensor apertures to remain contiguous, but it reduces the effective dynamic range on account of the amplifier that is required to read the acquired signal off the photosensor array chip. Very recently, analog VLSI capacitor networks have been exploited⁵⁵ in connection with IR imaging systems. Significant advances have been made in the rapidly developing technology of analog VLSI image processors since the last review⁵⁶ of its history. Digital VLSI processors, by comparison, sacrifice the power and wiring economies inherent in analog VLSI by orders of magnitude,⁵⁷ but gain in flexibility, stability, and accuracy.⁵⁸

Thus far, analog VLSI implementations have considered only spatial summations and differences, and a limited set of nonlinear intensity transformations (mainly logarithmic). Whether this technology will prove to be flexible enough to encompass other vision computations is a key question for future research. Perhaps the future of analog VLSI will be best guaranteed if it proves to be capable of the computations that provide a sort of universal front-end processing that supports a wide array of subsequent more specialized visual computations. To the extent that analog VLSI can mimic early natural vision, some confidence is justified that it is providing a generic foundation upon which a variety of diverse vision systems can be based. Even if analog VLSI is successful for universal vision-primitive computation, digital processing will almost certainly enter the system design for subsequent processing.

4 Performance

4.1 Small-Signal Linear Analysis

Figure 15 characterizes the information capacity \mathcal{H}_c and the maximum realizable fidelity \mathcal{F} as functions of the SFR $\hat{\tau}(v, \omega; \xi, \zeta)$ and the SNR $K\sigma_t/\sigma_p$ at the photosensor output (i.e., before quantization). The SFR, in turn, is controlled by the optical-response index ξ and the lateral-inhibition index ζ (Fig. 13). As the curves for \mathcal{H}_c reveal, the information capacity depends critically on ξ (i.e., on the trade-off between aliasing and blurring) as a function of the SNR, consistent with its dependence on the optical-design index $\gamma/2\lambda F$ as shown in Figs. 8 and 9. This dependence becomes now intuitively appealing in terms of the restoration of fine detail near the sampling lattice. At one extreme, when the SNR is low, one would prefer to avoid substantial blurring because the noise constrains the restoration. At the other extreme,

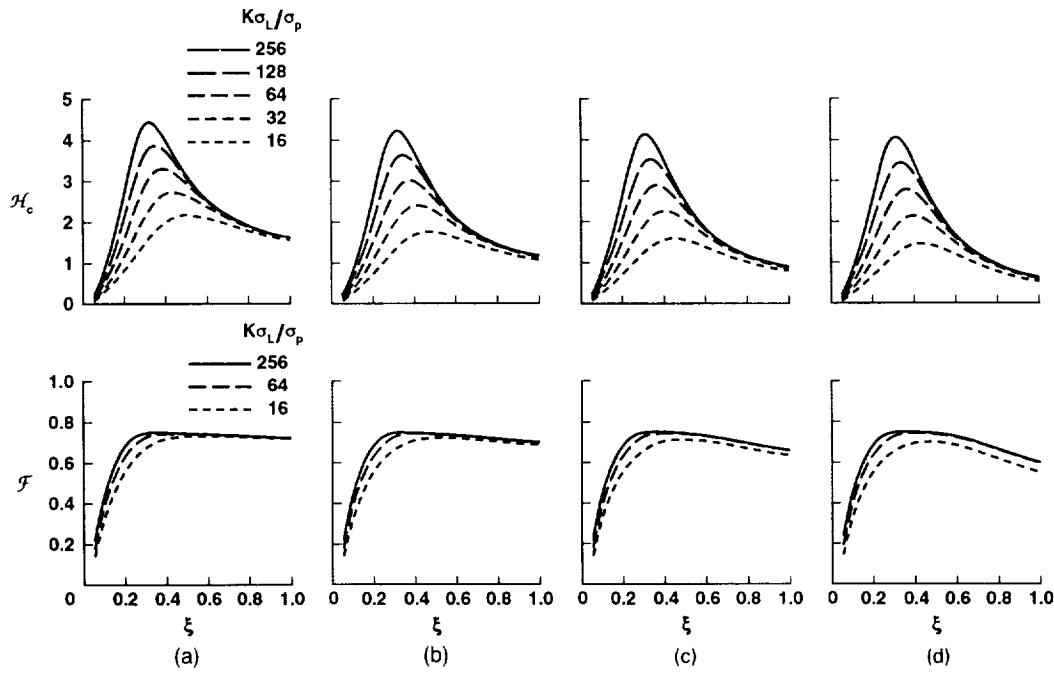


Fig. 15 Information capacity \mathcal{H}_c and maximum realizable fidelity \mathcal{F} as functions of the optical-response index ξ for several SNRs $K\sigma_L/\sigma_p$. The lateral inhibition is (a) $\zeta = 0$, (b) $\zeta = 0.6$, (c) $\zeta = 0.8$, and (d) $\zeta = 0.9$.

when the SNR is high, one would prefer to avoid substantial aliasing because the noise is no longer a constraint.

The curves for \mathcal{H}_c also reveal that the loss of information with increasing lateral inhibition is small for image-gathering devices with SFRs (e.g., $\xi = 0.3$) and SNRs ($K\sigma_L/\sigma_p = 256$) that provide a high information capacity, but that it is large for devices with the conventional SFR (i.e., $\xi = 0.8$) regardless of the SNR. Finally, the curves for both \mathcal{H}_c and \mathcal{F} reveal that the optical design that maximizes \mathcal{H}_c also maximizes the fidelity \mathcal{F} . Again, the loss of fidelity, like that of information, is small for a device with a high \mathcal{H}_c and comparatively large for a device with a low \mathcal{H}_c . Therefore, it is for the conventional design that one can expect lateral inhibition to impair the restoration of fine detail most severely.

Figure 16 characterizes the information capacity \mathcal{H}_c and information efficiency $\mathcal{H}_c/\mathcal{E}$ as functions of the number of quantization levels. Lateral inhibition is not included. The selection of quantization levels given in Table 2 for the two informationally optimized designs favors information capacity. A smaller number of quantization levels for these two designs would increase the information efficiency, but only at the cost of information and fidelity. However, for commercial digital imaging systems, as characterized by design 1, the 8-bit quantization could be reduced to 5-bit quantization to increase the information efficiency without loss in the information capacity. In practice, the preferred η -bit quantization can be matched to the standard 8-bit (or 12-bit) format of commercial codec (encoder/decoder) methods, such as JPEG, simply by assigning the coarse quantizations for $\eta = 7, 6$, and 5 to every second, fourth, or eighth level, respectively, of the 8-bit standard.

Figure 17 characterizes the dynamic range compression $\sigma_{\zeta}^2/\sigma_{s0}^2$, the information capacity \mathcal{H}_c , and the information

efficiency $\mathcal{H}_c/\mathcal{E}$ as functions of the lateral-inhibition index ζ for the three designs specified in Table 2. The dynamic range compression is given by the ratio

$$\frac{\sigma_{\zeta}^2}{\sigma_{s0}^2} = \frac{\iint_{-\infty}^{\infty} \hat{\Phi}_L(\nu, \omega) |\hat{\tau}(\nu, \omega; \xi, \zeta)|^2 d\nu d\omega}{\iint_{-\infty}^{\infty} \hat{\Phi}_L(\nu, \omega) |\hat{\tau}(\nu, \omega; \xi, 0)|^2 d\nu d\omega} \quad (22)$$

By suppressing the low SFR, lateral inhibition decreases the within-passband signal components relative to the aliased signal components (see Fig. 13). Consequently, the interference from aliasing increases strongly as the optical response index ξ increases beyond 0.4 while the lateral-inhibition index ζ approaches 1. It is therefore not surprising that, as lateral inhibition increases, \mathcal{H}_c and $\mathcal{H}_c/\mathcal{E}$ decrease significantly for design 1, modestly for design 2, and negligibly for design 3. For design 2, $\zeta = 0.7$ provides a dynamic range compression ≈ 4 and reduces the information capacity to $\mathcal{H}_c \approx 3$ bifs; and for design 3, the lateral inhibition with $\zeta = 0.8$ provides a dynamic range compression ≈ 5 and reduces the information capacity to $\mathcal{H}_c \approx 4$ bifs. Both designs 2 and 3 represent reasonable alternatives; the choice between them depends mostly on the SNR that can be attained.

Figure 18 presents Wiener restorations for the three designs specified in Table 2. The lateral-inhibition index is either $\zeta = 0$ or 0.8. Consistent with the curves for \mathcal{H}_c and \mathcal{F} in Fig. 15, design 2 significantly improves on the resolution and clarity attained with the conventional design 1. The improvement in visual quality for design 3 over that for design 2 is relatively small. This improvement requires significantly higher SNR but not a higher data rate. Note, in particular, that the lateral inhibition does not perceptibly impair the visual quality for the two optimized designs, whereas it im-

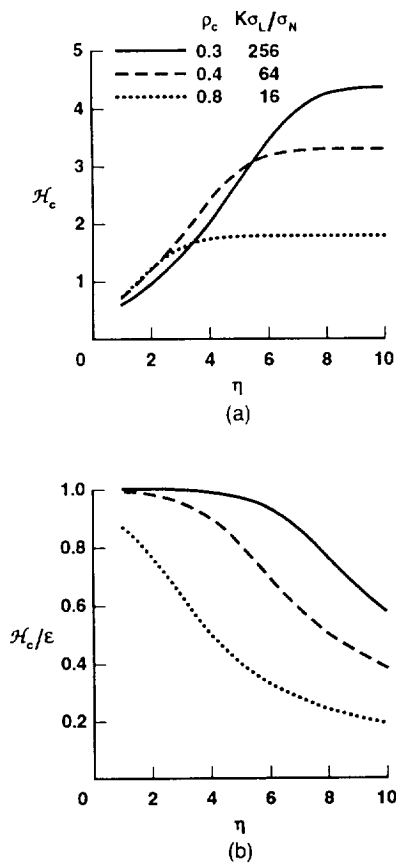


Fig. 16 Information capacity H_c and information efficiency H_c/ϵ as functions of the number of quantization levels η .

Table 2 Characteristics of conventional and informationally optimized image gathering for $\mu = 1$.

Design	ξ	$K\sigma_L/\sigma_N$	η , bits	H_c , bifs	ϵ , bits	H_c/ϵ
1 Conventional	0.8	16	8(5)*	1.8	7.5(4.6)	0.24(0.39)
2 Optimized	0.4	64	7	3.3	5.6	0.59
3 Optimized	0.3	256	8	4.2	5.6	0.75

*5-bit quantization may often be sufficient for the low information capacity H_c of this design.

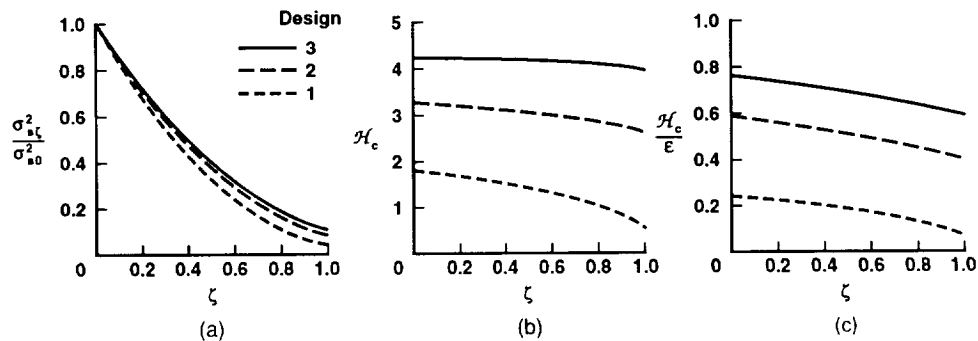


Fig. 17 Characteristics of image gathering with lateral inhibition for the three designs specified in Table 1: (a) dynamic range compression, (b) information capacity, and (c) information efficiency.

pairs the already poorer visual quality for the conventional design even further. Moreover, the theoretical minimum data rate for the two optimized designs is a factor of 1.3 lower than for the conventional design. Thus, the informationally optimized design offers a lower data rate in addition to better image quality and more robust dynamic-range compression.

4.2 Large-Signal Nonlinear Analysis

Image gathering with nonlinear conversion can be included in Eqs. (1) by replacing the linear gain K with the nonlinear gain $K(\alpha)$. In practice, the nonlinearity is commonly introduced in the analog-to-digital converter, i.e., after sampling rather than before. However, the order of nonlinear conversion and sampling can be interchanged mathematically. Moreover, the nonlinear conversion affects mostly the wide dynamic range of the low-spatial-frequency components of the radiance field without significantly distorting the high-spatial-frequency detail that one wishes to enhance. Therefore, in practice one can often interchange the order of nonlinear conversion and spatial convolution without introducing serious errors.⁵⁹

A common nonlinear conversion is given by the power relationship⁵⁹

$$s_0 = (\kappa - 1)^{1-1/\alpha} s^{1/\alpha}, \quad (23)$$

which is illustrated in Fig. 19. This nonlinearity increases the quantization density in the dark portions of the radiance field at the expense of reducing it in the bright portions. For $\alpha = 2$, this relationship becomes the "square-root" coding often found in image encoding and models of nonlinear responses in human vision.⁶⁰

Figure 20 depicts three irradiance profiles that span the width of the random target. The variation in the irradiance is such that the average radiance field, as it would be measured by a light meter, remains constant. The irradiance of the shadowed region is a factor of either 5, 25, or 125 lower than that of the bright region. These ratios encompass the variations in the depth of terrestrial shadows that one commonly encounters.

Figure 21 characterizes the radiance field that is the product of the reflectances of the random target and the three irradiances. It also characterizes the corresponding histograms of the radiance field and acquired signal, and the images restored from this signal. Results are given for design 2 as specified in Table 2. The restorations include histogram

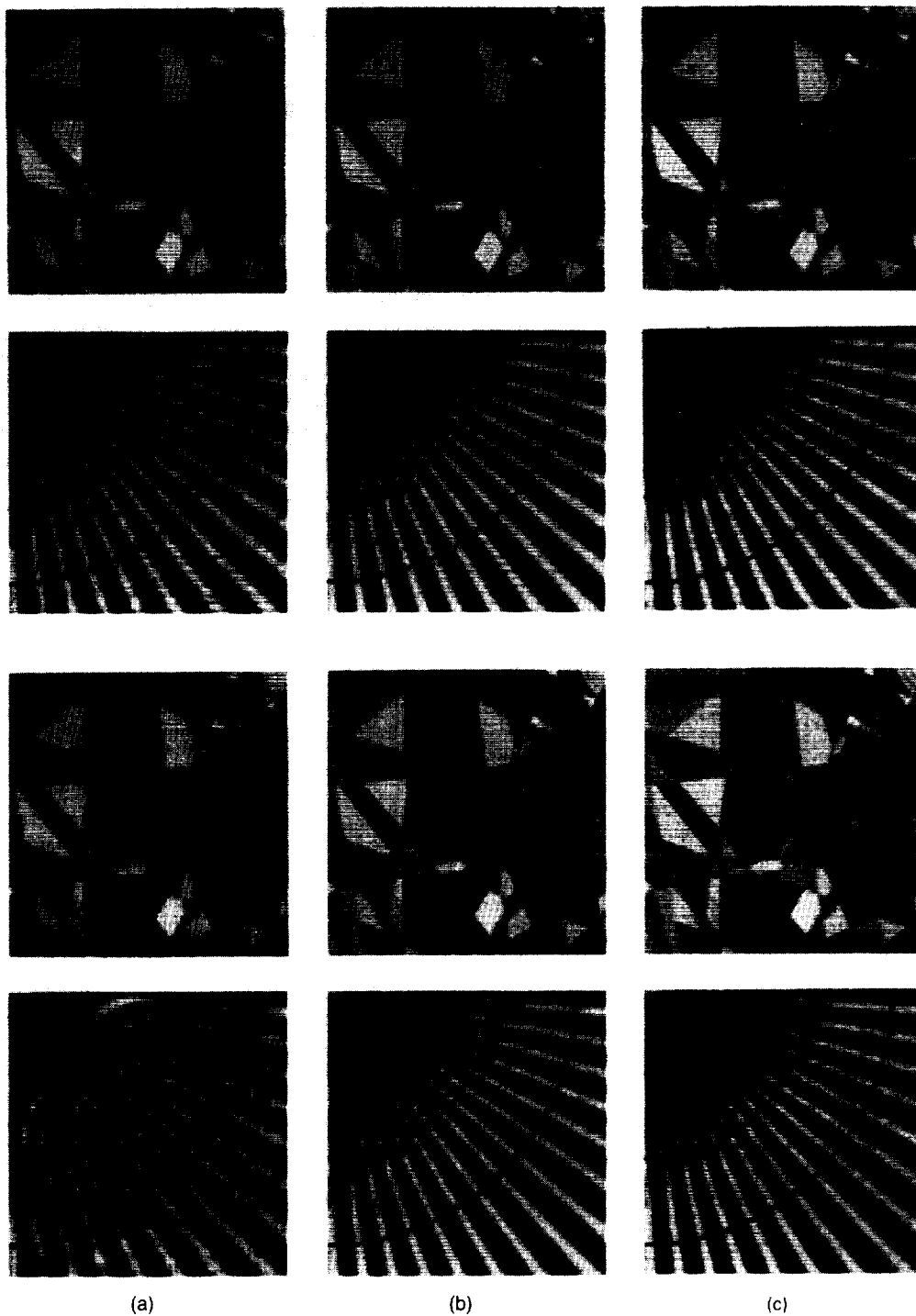


Fig. 18 Wiener restorations for (a) design 1, (b) design 2, and (c) design 3 characterized in Table 1. The amount of lateral inhibition is $\zeta = 0$ for the upper two rows and $\zeta = 0.8$ for the lower two rows.

equalization and edge enhancement. The latter is obtained by letting the SFR $\hat{\tau}(v, \omega; \xi, \zeta)$ in the Wiener filter given by Eq. (2) be $\hat{\tau}(v, \omega; \xi, \zeta = 0)$ regardless of the value of ζ that is actually used. In general, it is desirable to increase both non-linearity and lateral inhibition as the shadow deepens. It is then possible to resolve much of the structure of the scene in the displayed image, even when the radiance field with

the deep 125 : 1 shadow is compressed into the narrow 10 : 1 dynamic range of the image display.

It may be noted that the SNR for the average value of the spatially varying irradiance was kept the same as for the uniform irradiance, i.e., $K\sigma_I/\sigma_p = 64$. Consequently, the actual SNR in the shadowed region is a factor of 3 lower than this value for the 5 : 1 shadow, 13 for the 25 : 1 shadow,

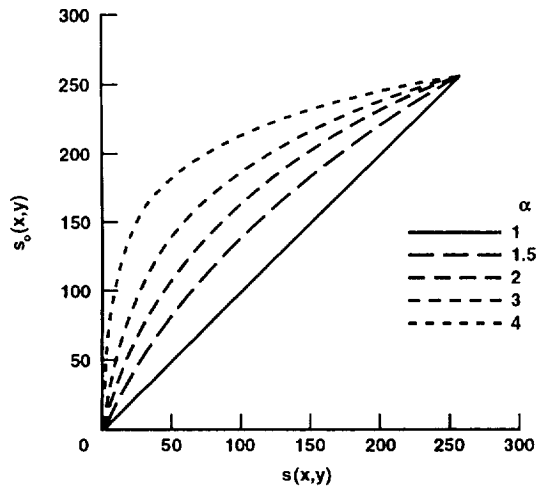


Fig. 19 Nonlinear radiance-to-signal conversion for $\kappa = 256$.

and 63 for the 125 : 1 shadow. For the deepest shadow, therefore, the SNR is only about unity. Yet the visual quality of the restored images is not perceptibly impaired by noise. This apparent robustness to noise results from the dynamic-range compression of the noise as well as of the signal variations by the nonlinearity of the film, which compresses the contrast of dark and bright levels near the limits of its dynamic range. However, if the spatial details in the shadowed region are displayed with improved contrast (at the cost of overexposing the bright region), then the need for a higher SNR becomes immediately apparent.

5 Concluding Remarks

The electro-optical design of the image-gathering device sets an upper bound on both the angular resolution and the information capacity of visual communication systems. The information capacity, in turn, sets upper bounds on the efficiency with which information can be transmitted and the visual quality with which images can be restored.

The electro-optical design trade-offs involve a large number of design variables and hence a wide range of design options. Nevertheless, if these trade-offs are optimized along guidelines developed from communication theory, then they lead inexorably to a design that is very similar to that of the human eye. The performance with this design approaches the maximum possible in terms of (1) the information capacity ($\mathcal{H}_c \approx 5$ bifs), (2) the information efficiency ($\mathcal{H}/\mathcal{E} = 0.8$ bifs/bit) of decorrelated data, and (3) the fidelity, sharpness, and clarity of the restored image. If lateral inhibition, akin to the retinal processing in the human eye, is included to reduce the wide dynamic range of natural radiance fields, then the information capacity for this design diminishes only slightly to $\mathcal{H}_c = 4.5$ bifs.

It may often be well worth while to use some of the clever mechanisms that the human eye employs to adapt to the wide depth of field and dynamic range that it commonly encounters:

1. As the pupil diameter increases to compensate for a decrease in scene illumination, aberrations increase to counter the associated decrease in diffraction blur. Our

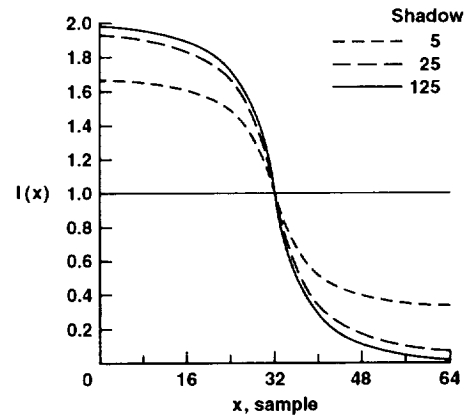


Fig. 20 Irradiance profiles across the random target.

results show that this increase in aberrations helps to maintain the informationally optimized relationship between the SFR of the optical (pupil and photoreceptor) apertures and the sampling passband of the photoreceptor lattice.

2. The angular sensitivity of the photoreceptors enhances the SFR and its robustness to defocus. The same enhancement can be produced by shading the objective lens with a variable transmittance.
3. The lateral inhibition in the retina acts like a second-order differentiator to enhance the radiance-field transitions relative to the low-spatial-frequency components. Our results show that this enhancement depends critically on the relationship between the SFR and sampling passband and that the preferred relationship is the one that maximizes the information capacity.
4. The dynamic-range compression in the retina occurs before the signal is converted to the pulses that are transmitted to the visual cortex. A similar implementation in the charge domain of the photosensor array, before a preamplifier reads the signal out to the analog-to-digital converter, could increase the effective dynamic range by an order of magnitude or more with little loss of information while decreasing the power required for digital processing by several orders of magnitude.

References

1. P. N. Slater, *Remote Sensing: Optics and Optical Systems*, Addison-Wesley, Reading, MA (1980).
2. R. W. Boyd, *Radiometry and the Detection of Optical Radiation*, Wiley, New York (1983).
3. F. O. Huck, H. F. McCall, W. R. Patterson, and G. R. Taylor, "The Viking Mars lander camera," *Space Sci. Instrum.* **1**, 189-241 (1975).
4. P. Mertz and F. Gray, "Theory of scanning and its relation to the characteristics of the transmitted signal in telephotography and television," *Bell Syst. Tech. J.* **13**, 494-515 (1934).
5. O. H. Schade, Sr., "Image gradation, graininess and sharpness in television and motion-picture systems," *J. Soc. Motion Pict. Telev. Eng.* **56**, 137-171 (1951); **58**, 181-222 (1952); **61**, 97-164 (1953); **64**, 593-617 (1955).
6. W. F. Schreiber, *Fundamentals of Electronic Imaging Systems*, Springer-Verlag, Berlin (1986).
7. H. C. Andrews and B. R. Hunt, *Digital Image Restoration*, Prentice-Hall, Englewood Cliffs, NJ (1977).
8. W. K. Pratt, *Digital Image Processing*, Wiley, New York (1978).
9. T. S. Huang, Ed., *Picture Processing and Digital Filtering*, Springer-Verlag, Berlin (1979).

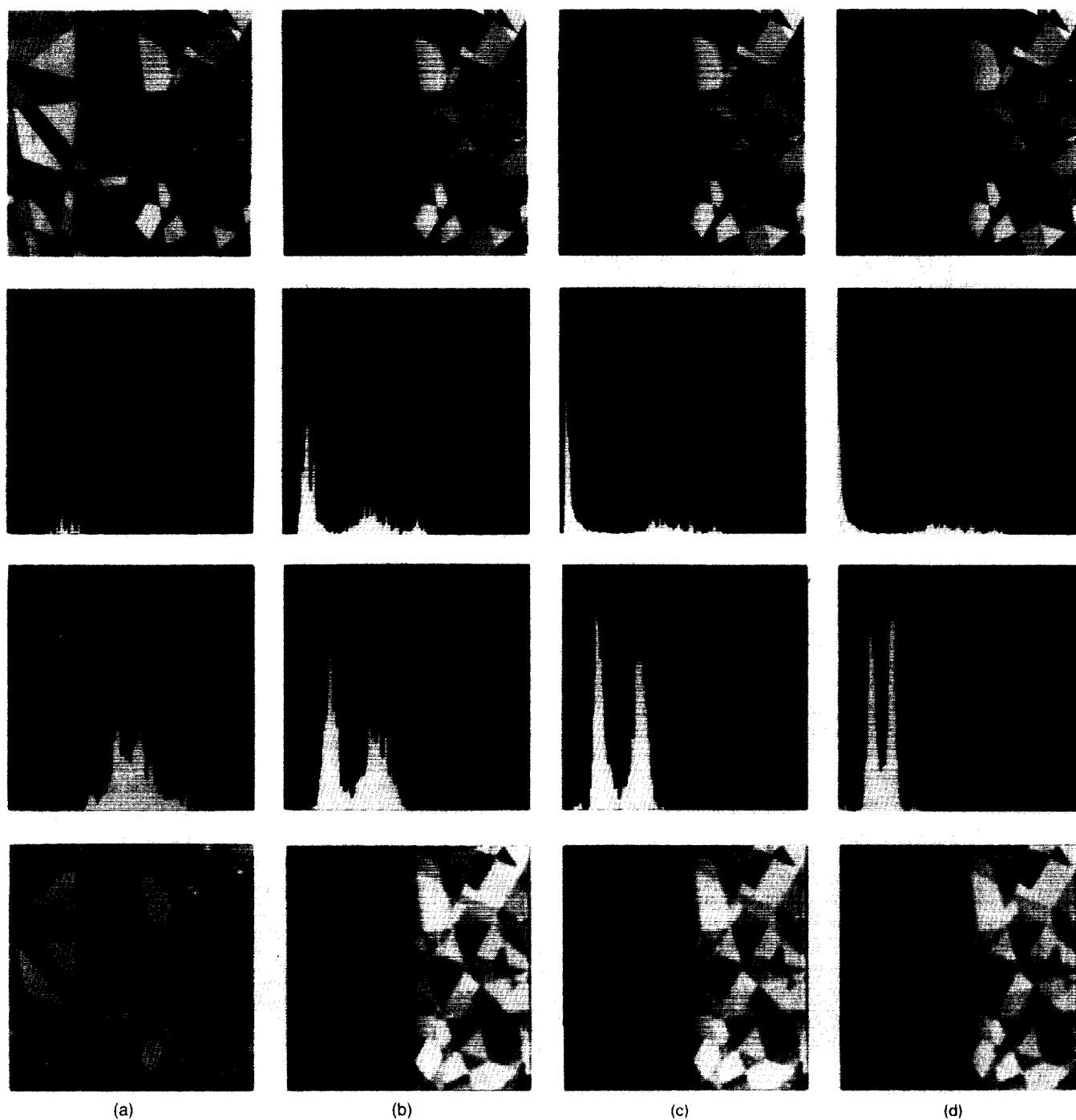
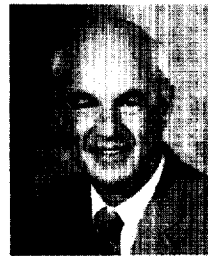
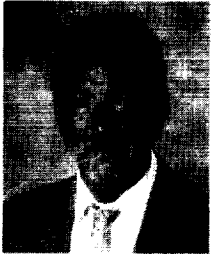


Fig. 21 Characteristics of the radiance field, acquired signal, and restored image for different irradiance profiles. Results are given for design 2 specified in Table 1. (a) Uniform irradiance, lateral inhibition $\zeta = 0$, and conversion $\alpha = 1$; (b) irradiance with 5 : 1 shadow, $\zeta = 0.6$, $\alpha = 1.5$; (c) irradiance with 25 : 1 shadow, $\zeta = 0.7$, $\alpha = 2.5$; (d) irradiance with 125 : 1 shadow, $\zeta = 0.8$, $\alpha = 3.5$. First row: radiance field. Second row: histogram of radiance field with dynamic range: (a) $25 \leq \kappa \leq 247$, (b) $12 \leq \kappa \leq 370$, (c) $5 \leq \kappa \leq 444$, (d) $0 \leq \kappa \leq 476$. Third row: histogram of signal with dynamic-range compression: (a) $37 \leq \kappa \leq 215$, (b) $14 \leq \kappa \leq 161$, (c) $10 \leq \kappa \leq 153$, (d) $0 \leq \kappa \leq 121$. Fourth row: restored images. The histograms are generated from a larger (1024×1024) target than the small (64×64) section for which the scene and images are shown.

10. A. Rosenfeld and A. C. Kak, *Digital Picture Processing*, Academic Press, New York (1982).
11. A. K. Jain, *Fundamentals of Digital Image Processing*, Prentice-Hall, Englewood Cliffs, NJ (1989).
12. R. C. Gonzalez and R. E. Woods, *Digital Image Processing*, Addison-Wesley, Reading, MA (1992).
13. C. L. Fales and F. O. Huck, "An information theory of image gathering," *Inform. Sci.* **57-58**, 245-285 (1991).
14. C. E. Shannon, "A mathematical theory of communication," *Bell Syst. Tech. J.* **27**, 379-423; **28**, 623-656 (1948); C. E. Shannon and W. Weaver, *The Mathematical Theory of Communication*, Univ. of Illinois Press, Urbana (1984).
15. N. Wiener, *Extrapolation, Interpolation, and Smoothing of Stationary Time Series*, Wiley, New York (1949).
16. F. O. Huck, C. L. Fales, R. Alter-Gartenberg, and Z. Rahman, "On the assessment of visual communication," in *Handbook of Statistics*, Vol. 10, N. K. Bose and C. R. Rao, Eds., pp. 383-397, North-Holland, Amsterdam, (1993).
17. F. O. Huck, C. L. Fales, R. Alter-Gartenberg, Z. Rahman, and S. E. Reichenbach, "Visual communication: information and fidelity," *J. Visual Comm. and Image Represent.* **4**, 62-78 (1993).
18. F. O. Huck, C. L. Fales, R. Alter-Gartenberg, and Z. Rahman, "Visual communication: information and data transmission," *J. Visual Comm. and Image Represent.* **5**, 282-300 (1994).
19. H. B. Barlow, "Critical limiting factors in the design of the eye and visual cortex," *Proc. R. Soc. London, Ser. B* **212**, 1-34 (1981).
20. C. Mead and M. A. Mahowald, "A silicon model of early visual processing," *Neural Networks* **1**, 91-97 (1988); C. Mead, *Analog VLSI and Neural Systems*, Addison-Wesley, Reading, MA (1989).
21. L. G. Roberts, "Picture coding using pseudorandom noise," *IRE Trans. Inform. Theory* **8**, 145-154 (1962).
22. S. E. Reichenbach and S. K. Park, "Small convolution kernels for high-fidelity image restoration," *IEEE Trans. Acoust. Speech Signal Process.* **ASSP-39**, 2263-2274 (1991).
23. Y. Itakura, S. Tsutsumi, and T. Takagi, "Statistical properties of the background noise for the atmospheric windows in the intermediate infrared region," *Infrared Phys.* **14**, 17-29 (1974).
24. M. Kass and J. Hughes, "A stochastic image model for AI," in *Proc. IEEE International Conf. on Systems, Man, and Cybernetics*, pp. 369-372, Inst. of Electrical and Electronics Engineers, New York (1983).
25. N. Ahuja and A. Rosenfeld, "Image models," in *Handbook of Statistics*, Vol. 2, P. R. Krishnaiah and L. N. Kanal, Eds., pp. 383-397, North-Holland, Amsterdam (1982).
26. J. W. Modestino and R. W. Fries, "Construction and properties of a useful two-dimensional random field," *IEEE Trans. Inform. Theory* **IT-26**, 44-50 (1980).
27. P. B. Fellgett and E. H. Linfoot, "On the assessment of optical images," *Philos. Trans. R. Soc. London* **247**, 369-407 (1955).
28. E. H. Linfoot, "Transmission factors and optical design," *J. Opt. Soc. Am.* **46**, 740-752 (1956).
29. R. Kingslake, *Optical System Design*, Academic Press, Orlando (1983).
30. W. J. Smith, *Modern Optical Engineering*, McGraw-Hill, New York (1990).
31. H. H. Hopkins, "The frequency response of a defocused optical system," *Proc. R. Soc. London, Ser. A* **231**, 91-103 (1955).
32. M. Born and E. Wolf, *Principles of Optics*, Pergamon, New York (1965).
33. J. W. Goodman, *Introduction to Fourier Optics*, McGraw-Hill, New York (1968).
34. M. Mino and Y. Okano, "Improvement in the OTF of a defocused optical system through the use of shaded apertures," *Appl. Opt.* **10**, 2219-2225 (1971).
35. C. L. Fales, F. O. Huck, and R. W. Samms, "Imaging system design for improved information capacity," *Appl. Opt.* **23**, 872-888 (1984).
36. J. M. Enoch and F. L. Tobey, Eds., *Vertebrate Photoreceptor Optics*, Springer-Verlag, New York (1981).
37. H. J. Metcalf, "Stiles-Crawford apodization," *J. Opt. Soc. Am.* **55**, 72 (1965).
38. J. P. Carroll, "Apodization model of the Stiles-Crawford effect," *J. Opt. Soc. Am.* **70**, 1155 (1980).
39. D. P. Peterson and D. Middleton, "Sampling and reconstruction of wave-number-limited functions in n -dimensional Euclidean spaces," *Inform. and Control* **5**, 279-323 (1962).
40. R. M. Mersereau, "Two-dimensional signal processing from hexagonal rasters," *Proc. IEEE* **67**, 930-949 (1979).
41. F. O. Huck, C. L. Fales, D. J. Jobson, S. K. Park, and R. W. Samms, "Image-plane processing of visual information," *Appl. Opt.* **23**, 3160-3167 (1984).
42. A. W. Snyder and W. H. Miller, "Photoreceptor diameter and spacing for highest resolving power," *J. Opt. Soc. Am.* **67**, 696-698 (1977).
43. R. L. Valois and K. K. Valois, *Spatial Vision*, Oxford Univ. Press, Oxford (1990).
44. P. Lennie, P. W. Haake, and D. R. Williams, "The design of chromatically opponent receptive fields," in *Computational Models of Visual Processing*, M. S. Landy and J. A. Movshon, Eds., MIT Press, Cambridge, MA (1991).
45. S. Goldman, *Information Theory*, Prentice-Hall, Englewood Cliffs, NJ (1953); Dover (1968).
46. M. J. Hawken and A. J. Parker, "Spatial receptive field organization in monkey V1 and its relationship to the cone mosaic," in *Computational Models of Visual Processing*, M. S. Landy and J. A. Movshon, Eds., MIT Press, Cambridge, MA (1991).
47. V. H. Perry, R. Oehler, and A. Cowey, "Retinal ganglion cells that project to the dorsal lateral geniculate nucleus in the macaque monkey," *J. Neurosci.* **12**, 1101-1123 (1984).
48. F. M. De Monasterio and P. Gouras, "Functional properties of ganglion cells of the rhesus monkey," *J. Physiol.* **251**, 167-195 (1975).
49. A. Hurlbert, "Formal connections between lightness algorithms," *J. Opt. Soc. Am. A* **3**, 1684-1692 (1986).
50. D. H. Hubel and M. S. Livingstone, "Color and contrast sensitivity in the lateral geniculate body and primary visual cortex of the macaque monkey," *J. Neurosci.* **10**, 2223-2237 (1990).
51. W. H. Merigan, "Chromatic and achromatic vision in macaques: role of the p pathway," *J. Neurosci.* **9**, 776-783 (1989).
52. D. C. Van Essen, D. M. Lam, and C. D. Gilbert, "Neural responses to moving texture patterns in visual cortex of the macaque monkey," in *Neural Mechanisms of Visual Perception*, Portfolio, Woodland, Tx (1989).
53. C. D. Gilbert and T. N. Wiesel, "The influence of contextual stimuli on the orientation selectivity of cells in the primary visual cortex of the cat," *Vision Res.* **30**, 1689-1701 (1990).
54. A. Moore, J. Allman, and Rodney M. Goodman, "A real-time neural system for color constancy," *IEEE Trans. Neural Networks* **2**, 237-247 (1991).
55. M. A. Massie, J. T. Woolaway, and J. P. Curzan, "Neuromorphic infrared focal plane performs sensor fusion on-plane local contrast enhancement spatial and temporal filtering," in *Visual Information Processing II, Proc. SPIE* **1961**, 160-174 (1993).
56. C. Koch, "Seeing chips: analog VLSI circuits for computer vision," *Neural Comput.* **1**, 184-200 (1989).
57. C. Mead, "Neuromorphic electronic system," *Proc. IEEE* **78**, 1629-1636 (1990).
58. D. D. Buss and G. L. Baldwin, "Comparative approaches to sampled-data signal processing: CCD vs all-digital," in *1976 IEEE Solid State Circuits Conference Digest of Technical Papers*, p. 172, IEEE, Lewis Winner, New York (1976).
59. W. F. Schreiber, "Image processing for quality improvement," *Proc. IEEE* **66**, 1640-1651 (1978).
60. J. Walraven, C. Enroth-Cugell, D. C. Hood, D. I. A. MacLeod, and J. W. Schnapf, "The control of visual sensitivity: receptor and postreceptor processes," in *Visual Perception, the Neurophysiological Foundations*, L. Spillmann and J. S. Werner, Eds., pp. 53-101, Academic Press, New York (1990).

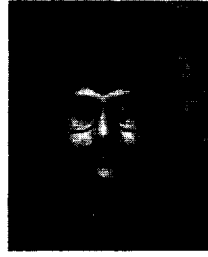


Friedrich O. Huck is a senior research engineer at NASA Langley Research Center. He received a MS in electrical engineering from the University of Rhode Island in 1963. He has been a member of the Lunar Orbiter project, a science team member of the Viking/Mars lander imaging investigation, and a principal investigator of the ERBE (Earth Radiation Budget Experiment) mission. For the Lunar Orbiter mission, he developed the imaging strategy for photographing potential Apollo landing sites. For the Viking/Mars mission, he participated in the design of the lander cameras and developed the imaging strategy for photographing the lander sites. And for the ERBE mission, he participated in the design of the spacecraft sensors and developed a computational model of the measurement process to enable and validate highly accurate dynamic radiometric measurements. More recently, he has been increasingly involved in extending Shannon's communication theory to visual communication as a whole, combining electro-optical design with digital image processing. He is currently a group leader concerned with the commercialization of remote sensing, using high-resolution imagers and imaging spectrometers, for the efficient inventory of Earth resources. He shared the 1977 Goddard Trophy with the other Viking project team members and the 1977 Newcomb Cleveland Prize of the American Association for the Advancement of Science with the other Viking scientists. He also received the NASA medals for exceptional service and exceptional engineering achievement.



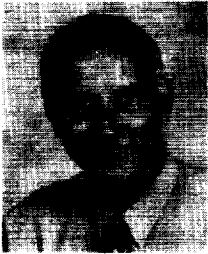
Carl L. Fales is a senior research engineer at NASA Langley Research Center. He received an MS in electrical engineering from North Carolina University in 1964, and a PhD in physics from the College of William and Mary in 1975. He performed theoretical studies and instrument developments for a wide range of aerospace applications. This includes the study of radiation effects on Lunar Orbiter electronics, the design and development of diagnostic

instrumentation that enabled the reliable manufacturing of the memory planes for the Viking lander computer, the design and development of a miniature electro-optical head for airplane oculometers, and the characterization of the wavelength accuracy of laser wave-meters. More recently, he has been increasingly involved in extending Shannon's communication theory to visual communication as a whole, combining electro-optical design with digital image processing. He is currently applying this mathematical approach to the development of commercial remote sensing, using high-resolution imagers and imaging spectrometers, for the efficient inventory of Earth resources.



Zia-ur Rahman is a research scientist with the Science and Technology Corporation, and is presently working under contract to NASA Langley Research Center on advanced concepts in information processing for high-resolution imaging and imaging spectrometry. He received a BA in physics from Ripon College in 1984, and an MS and a PhD in electrical engineering from the University of Virginia in 1986 and 1989, respectively. His graduate research fo-

cused on using neural networks and image-processing techniques for motion detection and target tracking. Currently he is involved in conducting research in multidimensional signal processing, with an emphasis in data compression and feature extraction methods. This work supports a NASA project for providing readily accessible, inexpensive remote-sensing data. He is a member of IEEE and INNS.



Daniel J. Jobson is a senior research scientist at NASA Langley Research Center. He received his BS in physics from the University of Alabama in 1969. Mr. Jobson's research has spanned topics including the design and calibration of the Viking/Mars lander camera, the colorimetric and spectrometric characterization of the two lander sites, the design and testing of multispectral sensors, and the analysis of coastal and ocean properties from re-

motely sensed data. For the past several years, his research interest has been in visual information processing with emphasis on machine vision analogs for natural vision, focal-plane processing technology, and nonlinear methods that mimic the dynamic-range-lightness constancy of human vision.